## Fragility of gate-error metrics in simulation models of flux-tunable transmon quantum computers

H. Lagemann, <sup>1,2,\*</sup> D. Willsch, <sup>1</sup> M. Willsch, <sup>1,3</sup> F. Jin, <sup>1</sup> H. De Raedt, <sup>1,4</sup> and K. Michielsen <sup>1,2,3</sup>

<sup>1</sup> Jülich Supercomputing Centre, Institute for Advanced Simulation,
Forschungszentrum Jülich, 52425 Jülich, Germany

<sup>2</sup> RWTH Aachen University, D-52056 Aachen, Germany

<sup>3</sup> AIDAS, 52425 Jülich, Germany

<sup>4</sup> Zernike Institute for Advanced Materials,
University of Groningen, Nijenborgh 4, NL-9747 AG Groningen, The Netherlands

(Dated: January 5, 2024)

Constructing a quantum computer requires immensely precise control over a quantum system. A lack of precision is often quantified by gate-error metrics, such as the average infidelity or the diamond distance. However, usually such gate-error metrics are only considered for individual gates, and not the errors that accumulate over consecutive gates. Furthermore, it is not well known how susceptible the metrics are to the assumptions which make up the model. Here, we investigate these issues using realistic simulation models of quantum computers with flux-tunable transmons and coupling resonators. Our main findings reveal that (1) gate-error metrics are indeed affected by the many assumptions of the model, (2) consecutive gate errors do not accumulate linearly, and (3) gate-error metrics are poor predictors for the performance of consecutive gates. Additionally, we discuss a potential limitation in the scalability of the studied device architecture

Keywords: Quantum Computation, Quantum Theory, Mesoscale and Nanoscale Physics, Superconductivity, Flux-tunable Transmons, Gate errors

#### I. INTRODUCTION

The realisation of a gate-based quantum computer in the real world is an engineering task which requires a tremendous amount of precision in terms of control over a quantum system. In this work we will clearly differentiate between the following three concepts: the ideal gate-based quantum computer (IGQC), the prototype gate-based quantum computers (PGQCs) and the non-ideal gate-based quantum computers (NIGQCs).

The state of an IGQC with  $N \in \mathbb{N}$  qubits is described by a time-independent state vector  $|\psi\rangle$  in a  $2^N$  dimensional Hilbert space as described in Refs. [1, 2]. In this model changes of the state vector occur instantaneously by applying unitary operators  $\hat{U}$  to the state vector  $|\psi\rangle$ . Therefore, all time-dependent aspects of gate errors which are omnipresent on PGQCs, see Ref. [3, 4], are neglected in this model. One often uses quantum operations, see Refs. [1, 2], to introduce gate errors to the IGQC model. Many gate-error metrics like the average gate infidelity, see Refs. [5, 6] and the diamond distance, see Refs. [7, 8], can be expressed in terms of quantum operations. However, also quantum operations do not describe the time-dependent aspects of gate errors.

In this work, we are interested in modelling the appearance of gate errors as a real-time process. This type of modelling is motivated by the fact that superconducting PGQCs are physical systems and consequently one finds that these devices are inherently dynamic and af-

fected by various internal and external factors. A review of the literature suggests that we have to take into account the variable control signals, see Ref. [9, 10], the temperature of the device, see Ref. [11], temporal stability of device parameters like the qubit frequency, see Ref. [12], cosmic radiation, see Ref. [13] and so on. Therefore, a complete mathematical description of these devices which takes into account all the relevant factors in one mathematical model seems prohibitive. However, we may be able to describe certain aspects of a superconducting PGQC by making use of simplified models. The simulations we perform to obtain the results presented in this work are intended to describe certain aspects of specific two-qubit, three-qubit and four-qubit superconducting PGQCs. The device architecture, device parameters and control pulses we use are similar to the ones used in experiments described in Refs. [14–16].

We define a NIGQC model as a model where the state of a gate-based quantum computer is described as a real-time entity. In this work, the state of a NIGQC is by assumption completely determined by the state vector  $|\Psi(t)\rangle$  and the dynamics of the system are generated by the time-dependent Schrödinger equation with  $\hbar=1$ 

$$i\partial_t |\Psi(t)\rangle = \hat{H}(t) |\Psi(t)\rangle,$$
 (1)

where  $\hat{H}(t) = \hat{H}^{\dagger}(t)$  denotes a circuit Hamiltonian which is obtained by means of the lumped-element approximation, see Ref. [17, Section 1.4] and an associated effective Hamiltonian, see Ref. [18]. Note that the NIGQC models that we consider are idealised versions of the PGQCs used in experiments.

Our simulation software solves the time-dependent Schrödinger equation numerically with the product-

<sup>\*</sup> Corresponding author: hannes.a.l@me.com; Published by Phys. Rev. A as Phys. Rev. A 106, 022615 (2023)

formula algorithm, see Refs. [19, 20], for a given Hamiltonian  $\hat{H}(t)$  and a sequence of control pulses which allows us to implement a sequence of gates with our NIGQC. This enables us to compute the gate errors for the individual gates in the program sequence. In the following, we call the sequence of gate errors which arises from this procedure a gate-error trajectory.

This manuscript is structured as follows. First, in Sec. II we specify the Hamiltonians H(t), the device parameters and the control pulses we use to implement our NIGQC models. Second, in Sec. III we discuss the gate-error metrics and how we compute them. Third, in Sec. IV we present our findings. In Sec. IV A, we discuss the spectrum of a four-qubit NIGQC and its relevance for the gate-error metrics we compute. Next, in Sec. IVB, we discuss the gate-error metrics we obtained by optimising the parameters of the control pulses. Then, in Sec. IV C we show how gate-errors and the corresponding gate-error trajectories which arise over time are affected by modelling the dynamics of the system with different numbers of basis states. The gate errors in this section are obtained with the circuit Hamiltonian. Next, in Sec. IVD we show how deviations in the control pulse parameters affect the gate-error trajectories. The gate errors in this section are also obtained with the circuit Hamiltonian. Then, in Sec. IV E we show how the modelling of flux-tunable transmons as adiabatic and nonadiabatic anharmonic oscillators affects the gate errors over time. The gate errors in this section are obtained with an effective Hamiltonian. A summary, discussion and the conclusions drawn are presented in Sec. V. Note that we use  $\hbar = 1$  throughout this work.

To assist the reader in navigating through the material, we list the main findings:

- 1. The authors of Refs. [3] concluded that the initial values for gate-error metrics like the diamond distance and the average infidelity are poor predictors of the future gate-error trajectories which emerge over time. In this work we provide new evidence which supports and strengthens this conclusion. Furthermore, we provide a concise theoretical explanation for why this is the case and how we should interpret gate-error metrics like the diamond distance and the average infidelity, see Secs. IV C–IV E.
- 2. By analysing the spectrum of a four-qubit NIGQC, we discuss a problem which potentially limits the up-scaling capabilities of device architectures which implement two-qubit gates by tuning the energies of basis states into resonance with one another. The issues we discuss implicate an exponentially large optimisation problem for future quantum computer engineers, see Sec. IV A.
- 3. By simulating the time evolution of different NIGQC models, we explicitly show that even seemingly small changes in the assumptions which make

up the underlying model can substantially affect the gate-error metrics. The fact itself is not surprising. However, the extent to which the changes affect the gate-error metrics during the course of the time evolution of the system is something worth knowing, see Secs. IV C-IV E.

4. By executing simple gate repetition programs on different NIGQCs, we show that gate-error metrics in NIGQC models do not behave linearly. Furthermore, we also show that gate-error metrics respond to changes in the model in a non-linear manner, see Secs. IV C-IV E. Given these findings we conjecture that gate errors for consecutive gates are not simply given by the sum of the gate errors for the individual gates in the program sequence but emerge due to a complex interplay of small deviations with respect to the target gates which occur over time.

#### II. MODELS AND DEVICE PARAMETERS

Figures 1(a-c) show illustrations of the two-qubit(a), three-qubit(b) and four-qubit(c) NIGQCs we consider in this work. The parameters  $\omega^{(Q)}$  denote the park qubit frequencies for the different flux-tunable transmon qubits. The park qubit frequency is the frequency at which a transmon qubit resides if no external flux is applied. Similarly, the parameters  $\omega^{(R)}$  refer to LC resonator frequencies. In the following, we will simply call these systems transmon qubits and resonators. The interactions between the different transmon qubits are conveyed by the resonators. We model the interactions between the different subsystems as dipole-dipole interactions and use the constants  $G_{i,j}$ , where  $i,j \in \mathbb{N}^0$ , to control the interaction strength. The device parameters listed in Table I are used for all simulations in this work.

The remainder of this section is devoted to the models we use to describe the dynamics of the NIGQCs in Figs. 1(a-c). In Sec. II A we introduce a circuit Hamiltonian. In Sec. II B we introduce an effective Hamiltonian which is related to the circuit Hamiltonian. Finally, in Sec. II C, we define the control pulses we use to implement the different gates.

The device architecture, device parameters and control pulses we use are motivated by experiments described in Refs. [14–16].

### A. The circuit Hamiltonian model

The circuit Hamiltonian we use to model our NIGQCs, is defined as

$$\hat{H}_{\text{Cir.}} = \hat{H}_{\text{Res.},\Sigma} + \hat{H}_{\text{Tun.},\Sigma} + \hat{V}_{\text{Int.}}.$$
 (2)

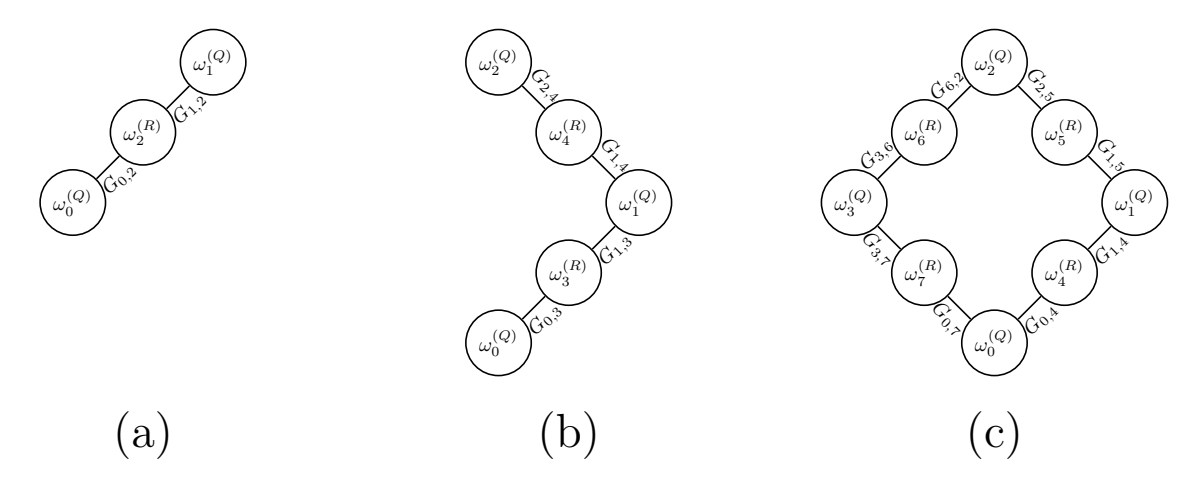


FIG. 1. Illustrations of flux-tunable transmon qubits with park qubit frequencies  $\omega^{(Q)}$  and resonators with resonance frequencies  $\omega^{(R)}$  which constitute non-ideal gate-based transmon quantum computers (NIGQCs) with N=2(a), N=3(b) and N=4(c) qubits. The different subsystems are indexed with the discrete variable  $i \in \{0,...,7\}$  such that the bare basis states of the system can be expressed as  $|\mathbf{z}\rangle$ , where  $\mathbf{z}=(z_{|I|-1},...,z_0)$  is an n-tuple. The Hamiltonians we use to model the dynamics of our NIGQCs are given by Eqs. (2) and (7). The device parameters we use to specify the Hamiltonians are listed in Table I. The control pulses we use to implement the gates are displayed in Figs. 2(a-c).

TABLE I. Device parameters for a four-qubit virtual chip. The device architecture and device parameters are motivated by experiments described in Refs. [14–16]. The index i denotes the different circuit elements which are part of the system (in total there are eight circuit elements). The parameter  $\omega_i^{(R)}$  denotes the coupler frequency, i.e. the transmission line resonator frequency. Since all couplers have the same frequency, we only show one row for all coupling resonators, see the last row where  $i \in \{4, 5, 6, 7\}$ . The constants  $\omega_i^{(Q)}$  and  $\alpha_i^{(Q)}$  denote the qubit frequency and anharmonicity, respectively.  $E_{C_i}$  denotes the capacitive energy of the i<sup>th</sup>qubit. Similarly,  $E_{J_i,r}$  and  $E_{J_i,l}$  denote the corresponding Josephson energies. Note that in this work we express the Hamiltonian in Eq. (4) with a factor of  $E_C$  instead of  $4E_C$ . This means we adopt the convention used in Ref. [21] and not the one of Ref. [22]. The parameter  $\varphi_{0,i}$  denotes the so-called flux offset, i.e. the external flux  $\varphi_{0,i}(t)$  at time t=0. The interaction strength  $G_{i,j}$  between the different circuit elements is set to 300 MHz for all  $i,j \in \mathbb{N}^0$ . All units (except the one of the flux offset) are in GHz. The flux offset is given in units of the flux quantum  $\Phi_0$ . We use these device parameters to model the two-qubit, three-qubit and four-qubit NIGQCs illustrated in Figs. 1(a-d). Note that we use  $\hbar=1$  throughout this work

i	$\omega_i^{(R)}/2\pi$	$\omega_i^{(Q)}/2\pi$	$\alpha_i^{(Q)}/2\pi$	$E_{C_i}/2\pi$	$E_{J_i,l}/2\pi$	$E_{J_i,r}/2\pi$	$\varphi_{0,i}/2\pi$
0	n/a	4.200	-0.320	1.068	2.355	7.064	0
1	n/a	5.200	-0.295	1.037	3.612	10.837	0
2	n/a	5.700	-0.285	1.017	4.374	13.122	0
3	n/a	4.960	-0.300	1.045	3.281	9.843	0
4 - 7	45.000	n/a	n/a	n/a	n/a	n/a	n/a

The first term,

$$\hat{H}_{\mathrm{Res.},\Sigma} = \sum_{k \in K} \omega_k^{(R)} \hat{a}_k^{\dagger} \hat{a}_k, \tag{3}$$

describes a collection of non-interacting resonators. Here  $K \subseteq \mathbb{N}^0$  denotes an index set for the resonators and  $\omega_k^{(R)}$  refers to the different resonator frequencies. The operators  $\hat{a}$  and  $\hat{a}^{\dagger}$  are the bosonic annihilation and creation operators, respectively.

Similarly, the second term,

$$\hat{H}_{\text{Tun.},\Sigma} = \sum_{j \in J} \left( E_{C_j} \left( \hat{n}_j - n_j(t) \right)^2 + \left( \frac{1}{2} - \beta_j \right) \dot{\varphi}_j(t) \hat{n}_j \right.$$

$$\left. - E_{J_{l,j}} \cos \left( \hat{\varphi}_j + \beta_j \varphi_j(t) \right) - E_{J_{r,j}} \cos \left( \hat{\varphi}_j + (\beta_j - 1) \varphi_j(t) \right) \right),$$

$$(4)$$

describes a collection of non-interacting flux-tunable transmons. Here  $J \subseteq \mathbb{N}^0$  denotes an index set for the transmon qubits. Furthermore, the parameters  $E_{C_j}$ ,  $E_{J_{l,j}}$  and  $E_{J_{r,j}}$  denote the capacitive energies, the left Josephson energies and the right Josephson energies. Note that the Hamiltonian in Eq. (4) is often expressed with a factor  $4E_C$  instead of  $E_C$ . In this work we adopt

the convention used in Ref. [21] and not the one of Ref. [22]. The parameters  $\beta_j$  are not device parameters but determine the variables we use for the quantisation of the circuit. We use  $\beta_j = 1/2$  for all simulations in this work, cf. Refs. [23, 24]. In Appendix A we provide a detailed derivation of the Hamiltonian for a single flux-tunable transmon with a charge drive term. This derivation is motivated by the work in Ref. [23].

The device parameters in Table I were obtained as follows. The Quantum Device Lab which is affiliated with the ETH Zurich provided us with the qubit frequencies  $\omega_j^{(Q)}$ , anharmonicities  $\alpha_j^{(Q)}$  and asymmetry factors  $d_j$  for the various transmon qubits in the system as well as the coupling resonator frequencies  $\omega_k^{(R)} = 45$  GHz. We then used the relations

$$\omega_j^{(Q)} = (E_j^{(1)} - E_j^{(0)}), \tag{5a}$$

$$\alpha_i^{(Q)} = (E_i^{(2)} - E_i^{(0)}) - 2\omega_i^{(Q)},$$
 (5b)

$$d_j = \frac{E_{J_{r,j}} - E_{J_{l,j}}}{E_{J_{r,j}} + E_{J_{l,j}}},$$
 (5c)

and Hamiltonian Eq. (4) to fit the energy levels  $E_j^{(0)}$ ,  $E_j^{(1)}$  and  $E_j^{(2)}$  to the provided data. The third term

$$\hat{V}_{\text{Int.}} = \sum_{(k,j) \in K \times J} G_{k,j} \left( \hat{a}_k + \hat{a}_k^{\dagger} \right) \otimes \hat{n}_j, \tag{6}$$

describes dipole-dipole interactions between resonators and transmon qubits. Here  $G_{k,j}$  is a real-valued constant which is set to 300 MHz for all simulations in this work. This value for interaction strength constants  $G_{k,j}$  roughly reproduces the gate durations of around 100 ns which were found to be appropriate in the experiment.

For our simulations of Hamiltonian Eq. (2) we use the product-formula algorithm, see Ref. [19, 20] and what we call a bare basis. This bare basis is formed by the tensor product states of the harmonic oscillator and the transmon basis states, which are obtained for the external flux  $\varphi_j(t)$  at time t=0. In this manuscript, we model the dynamics of Hamiltonian Eq. (2) with four basis states for all resonators and most transmon qubits are modelled with sixteen basis states. Only the transmon qubit with the index i=0, see Figs. 1(a-c), is modelled with four basis states. Note that this transmon does not experience a flux drive. Therefore, we can model this transmon with four basis states only. There is one exception to this rule namely, the results in Sec. IV C are obtained with four and sixteen basis states for all transmon qubits.

### B. The effective Hamiltonian model

The approximations which are needed to obtain the effective Hamiltonian defined in this section are discussed in detail in Ref. [18]. Furthermore, the full effective model is defined in terms of twelve equations. In order

to provide a concise discussion of the effective model, we only discuss the most relevant relations. A more detailed discussion of the effective model with all twelve equations can be found in Appendix B.

The effective Hamiltonian we use to model our NIGQCs is defined by

$$\hat{H}_{\text{Eff.}} = \hat{H}_{\text{Res.},\Sigma} + \hat{H}_{\text{Tun.eff.},\Sigma} + \hat{D}_{\text{Charge},\Sigma} + \hat{\mathcal{D}}_{\text{Flux},\Sigma} + \hat{W}_{\text{Int.}}.$$
(7)

The second term,

$$\hat{H}_{\text{Tun.eff.},\Sigma} = \sum_{j \in J} \omega_j^{(q)}(t) \hat{b}_j^{\dagger} \hat{b}_j + \frac{\alpha_j^{(q)}(t)}{2} \left( \hat{b}_j^{\dagger} \hat{b}_j \left( \hat{b}_j^{\dagger} \hat{b}_j - \hat{I} \right) \right), \tag{8}$$

describes a collection of non-interacting flux-tunable transmons which are modelled as adiabatic, anharmonic oscillators in a time-dependent basis. The operators  $\hat{b}$  and  $\hat{b}^{\dagger}$  are the bosonic annihilation and creation operators, respectively. The functions  $\omega_j^{(q)}(t)$  and  $\alpha_j^{(q)}(t)$ , see Eqs. (B4) and (B7), denote the flux-tunable qubit frequency and anharmonicity, respectively. Note that the time dependence in both these functions is given by the external flux  $\varphi_j(t)$ . In this work, we use the series expansions obtained by the authors of Ref. [25] to approximate the lowest three energy levels of Hamiltonian Eq. (4) for the external flux values  $\varphi_j(t)$  at any given point in time.

The third term,

$$\hat{D}_{\text{Charge},\Sigma} = \sum_{j \in J} \Omega_j(t) \left( \hat{b}_j^{\dagger} + \hat{b}_j \right), \tag{9}$$

describes a charge drive. Here  $\Omega_j(t) \propto -2E_{C_j}n_j(t)$  and we approximate the charge operators  $\hat{n}_j$  by effective charge operators  $\hat{n}_{j,\text{eff.}}$  which can be expressed in terms of the bosonic operators, see Ref. [22].

The fourth term,

$$\hat{\mathcal{D}}_{\text{Flux},\Sigma} = \sum_{j \in J} \left( -i\sqrt{\frac{\xi_{j}(t)}{2}} \dot{\varphi}_{\text{eff.},j}(t) \left( \hat{b}_{j}^{\dagger} - \hat{b}_{j} \right) + \frac{i}{4} \frac{\dot{\xi}_{j}(t)}{\xi_{i}(t)} \left( \hat{b}_{j}^{\dagger} \hat{b}_{j}^{\dagger} - \hat{b}_{j} \hat{b}_{j} \right) \right),$$
(10)

describes a nonadiabatic flux drive. Here  $\dot{\varphi}_{\mathrm{eff.},j}(t) \propto \dot{\varphi}_{j}(t)$  and  $\dot{\xi}_{j}(t)/\xi_{j}(t) \propto \dot{\varphi}_{j}(t)$ . Note that  $\dot{\varphi}_{\mathrm{eff.},j}(t)$  and  $\xi_{j}(t)$  are given by Eq. (B10)(a,c). This term results from the fact that we model the effective flux-tunable transmon in a time-dependent basis. Consequently, for the time-dependent Schrödinger equation to stay form invariant, see Ref. [18], a time-dependent basis transformation term is needed.

The fifth term,

$$\hat{W}_{\text{Int.}} = \sum_{(k,j)\in K\times J} g_{k,j}^{(a,b)}(t) \left( \hat{a}_k^{\dagger} + \hat{a}_k \right) \otimes \left( \hat{b}_j^{\dagger} + \hat{b}_j \right), \tag{11}$$

describes time-dependent dipole-dipole interactions. The time dependence of the interaction strength is a result of

the fact that we model the effective flux-tunable transmon in a time-dependent basis, see Ref. [18]. The function  $g_{k,j}^{(a,b)}(t)$  is given by Eq. (B16). This time-dependent interaction strength model is motivated by the work in Ref. [22].

As before, we use the product-formula algorithm, see Ref. [19, 20], to solve the time-dependent Schrödinger equation for the Hamiltonian Eq. (7). Here we use a bare basis that is formed by the tensor product states of the time-independent (for the resonators) and time-dependent (for the transmon qubits) harmonic oscillator for the simulations. In this work, the dynamics of Hamiltonian Eq. (7) are modelled with four basis states for all resonators and transmons.

#### C. The control pulses and gate implementations

Figures 2(a-c) show the external charge n(t)(a) and the external flux  $\varphi(t)(b-c)$  as functions of time t. In (a) we show a microwave pulse (MP), in (b) we show a unimodal pulse (UMP) and in (c) we show a bimodal pulse (BMP). In this section we introduce the functions which are used to obtain the data we show in Figs. 2(a-c). We use these functions as control pulses for our NIGQC models.

For the single-qubit gates we use the external charge

$$n(t) = aG(t, \sigma, T_d) \cos \left(\omega^{(D)}t - \phi\right) + b\dot{G}(t, \sigma, T_d) \sin \left(\omega^{(D)}t - \phi\right),$$
(12)

to drive transitions that can be used to implement  $R^{(x)}(\pi/2)$  rotations with a microwave control pulse. Here  $G(t, \sigma, T_d)$  is a Gaussian envelope function centered around half of the pulse duration  $T_d$ . The width and the shape of the Gaussian are determined by the parameters  $\sigma$  and  $T_d$ . Furthermore, a denotes the pulse amplitude,  $\omega^{(D)}$  refers to the drive frequency, b is the amplitude of the DRAG pulse component, see Ref. [26], and  $\phi$  is the phase of the pulse. We use the phase  $\phi$  in Eq. (12) to implement virtual Z gates, see Ref. [27], on our NIGQCs.

Two-qubit CZ gates can be implemented with an external flux of the form

$$\varphi(t) = \frac{\delta}{2} \left( \operatorname{erf} \left( \frac{t}{\sqrt{2}\sigma} \right) - \operatorname{erf} \left( \frac{(t - T_p)}{\sqrt{2}\sigma} \right) \right),$$
(13)

where  $\delta$  denotes the pulse amplitude,  $\sigma$  is a parameter which allows us to control how fast the pulse flanks rise and fall,  $T_p$  is the pulse time, and erf denotes the Gauss error function. Note that in the computer program we add an additional free time evolution (the buffer time) to the pulse such that the complete pulse duration  $T_d$  is longer than  $T_p$ . We denote this pulse as the UMP.

We can also use the external flux

$$\varphi(t) = \frac{\delta}{2} \left( \operatorname{erf} \left( \frac{t}{\sqrt{2}\sigma} \right) - 2\operatorname{erf} \left( \frac{(t - T_p/2)}{\sqrt{2}\sigma} \right) + \operatorname{erf} \left( \frac{(t - T_p)}{\sqrt{2}\sigma} \right) \right), \tag{14}$$

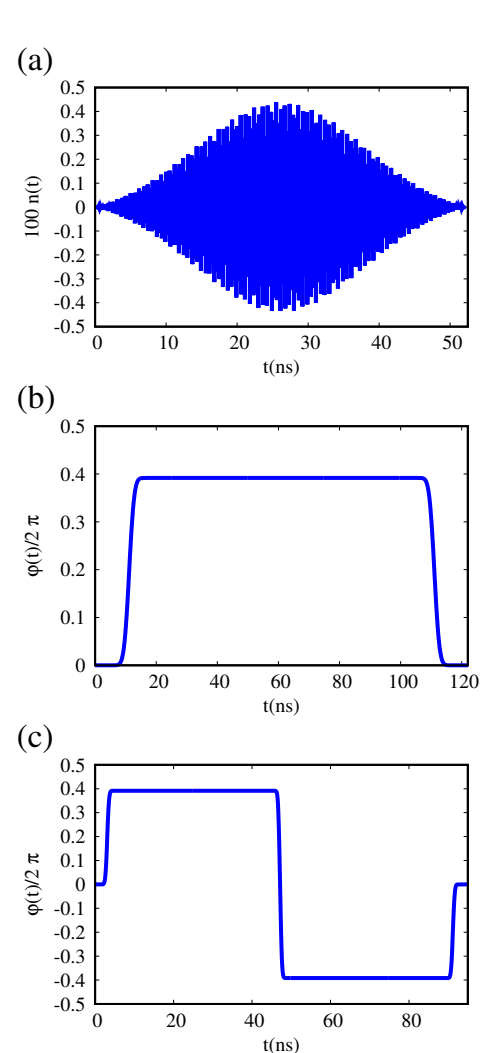


FIG. 2. (Color online) External charge n(t)(a) given by Eq. (12) and external fluxes  $\varphi(t)$ (b-c) given by Eqs. (13) and (14), respectively, as a functions of time t. (a) microwave pulse (MP); (b) unimodal pulse (UMP); (c) bimodal pulse (BMP). In the circuit model both functions n(t) and  $\varphi(t)$  enter via the Hamiltonian Eq. (4). In the effective model both functions n(t) and  $\varphi(t)$  enter via the driving terms Eqs. (9) and (10), respectively. Furthermore, in the effective model the external flux  $\varphi(t)$  also enters the time-dependent interaction strength in Eq. (11) and the tunable qubit frequency and anharmonicity in Eq. (8), see Appendix B for more details.

to implement two-qubit CZ gates. This pulse is referred to as the BMP. Note that the BMP pulse is sometimes referred to as net-zero flux pulse. The UMP and the BMP are also used to implement gates in experiments, see Refs. [9, 14-16].

Every CZ gate in our NIGQC model is implemented by means of a flux pulse  $\varphi(t)$  followed by single-qubit z-axis rotations  $R_i^{(z)}(\phi_i)$  for every qubit in the NIGQC model, see Ref. [28, Section VII B 2]. Since the z-axis rotation parameters  $\phi_i$  are quite numerous, e.g. a four-qubit system with four CZ gates has sixteen of these parameters, we omit the  $\phi_i$  phases from the control pulse parameter

Tables IX-XIX in Appendix D. Finally, we execute these z-axis rotations by means of virtual Z gates in combination with a transformation of the frame of reference which only affects the phases of the state vector but not the state vector amplitudes, see Ref. [29, Section 3.3.2].

### III. COMPUTATION OF GATE-ERROR QUANTIFIERS

In this section we discuss the gate-error quantifiers we compute as well as how we determine the numerical values.

A computation in the IGQC model can be understood as a mapping

$$|\psi\rangle \mapsto |\psi'\rangle$$
, (15)

between an initial state  $|\psi\rangle$  and a final state  $|\psi'\rangle$  and the state vector of an N-qubit IGQC can be expressed as

$$|\psi\rangle = \sum_{\mathbf{z} \in \{0,1\}^N} c_{\mathbf{z}} |\mathbf{z}\rangle,$$
 (16)

where  $\{|\mathbf{z}\rangle\}$  are the  $2^N$  computational basis states of the IGQC. All state vectors  $|\psi\rangle$  are normalised complex vectors in a finite dimensional Hilbert space  $\mathcal{H}^{2^N}$ . The computation is described by a unitary operator  $\hat{U}$ .

One simple error measure is the statistical distance

$$\mu_{\text{SD}}(\mathbf{p}, \tilde{\mathbf{p}}) = \frac{1}{2} \sum_{\mathbf{z} \in \{0,1\}^N} \|p_{\mathbf{z}} - \tilde{p}_{\mathbf{z}}\|_1,$$
(17)

where, by definition  $p_{\mathbf{z}} = \|\langle \mathbf{z} | \psi \rangle\|_1^2$  are the probability amplitudes of the IGQC (which we use as a reference distribution to compare against) and  $\tilde{p}_{\mathbf{z}}$  denote the actual distribution that is being evaluated. This distribution can either be generated by a PGQC or a NIGQC. Furthermore,  $\|\cdot\|_1$  denotes the absolute value. The advantage of the statistical distance is that we can more or less easily measure the relative frequencies  $p_{\mathbf{z}}$  in an experiment. While such an error measure is useful in practice, see Ref. [3, 4, 29], it neglects the phase information of the state vector  $|\psi\rangle$ . Furthermore, the statistical distance only provides a measure of closeness for one particular input state. For this reason, usually more sophisticated gate-error metrics are considered.

Most gate metrics are defined in terms of quantum operations. From a mathematical point of view, quantum operations are superoperators  $\check{\mathcal{E}}(\hat{\rho})$  which act on the space of density operators  $\hat{\rho} \in \mathcal{P}$ . Additionally, we require  $\check{\mathcal{E}}$  to be linear, Hermiticity preserving and completely positive, see Refs. [1, 2]. Note that if one can also show that  $\check{\mathcal{E}}$  is trace preserving,  $\check{\mathcal{E}}$  is usually referred to as quantum or error channel.

The error metrics we consider in this work can be expressed in terms of the two quantum operations

$$\check{\mathcal{E}}_{\mathrm{U}}(\hat{\rho}) = \hat{U}\hat{\rho}\hat{U}^{\dagger} \tag{18}$$

and

$$\check{\mathcal{E}}_{\mathcal{M}}(\hat{\rho}) = \hat{M}\hat{\rho}\hat{M}^{\dagger},\tag{19}$$

where  $\hat{\rho} = |\psi\rangle\langle\psi|$  and  $|\psi\rangle \in \mathcal{H}^{2^N}$ . The operator  $\hat{M}$  in Eq. (19) is defined as

$$\hat{M} = \hat{P}\hat{\mathcal{U}}(t, t_0)\,\hat{P},\tag{20}$$

where  $\hat{P}$  is a projection operator onto the computational space and  $\hat{\mathcal{U}}$  denotes the formal solution of the time-dependent Schrödinger equation

$$\hat{\mathcal{U}}(t,t_0) = \mathcal{T} \exp\left(-i \int_{t_0}^t \hat{H}(t')dt'\right). \tag{21}$$

Here  $\mathcal{T}$  is the time-ordering symbol. Furthermore, the Hamiltonian  $\hat{H}$  is either given by Eq. (2) or Eq. (7).

The first error metric that we consider is the average fidelity

$$\mu_{\mathrm{F}_{\mathrm{avg}}} = \int \langle \psi | \check{\mathcal{E}}_{\mathrm{M}} \check{\mathcal{E}}_{\mathrm{U}}^{-1} (|\psi\rangle\langle\psi|) |\psi\rangle d|\psi\rangle, \qquad (22)$$

where the integral is taken over all states  $|\psi\rangle \in \mathcal{H}^{2^N}$  in the Hilbert space. If we define the auxiliary operator

$$\hat{V} = \hat{U}\hat{M}^{\dagger},\tag{23}$$

we can express the average fidelity as

$$\mu_{\text{F}_{\text{avg}}} = \frac{\|\text{Tr}(\hat{V})\|_{1}^{2} + \text{Tr}(\hat{M}\hat{M}^{\dagger})}{D(D+1)},$$
(24)

where  $D = 2^N$ . This is expression is derived in Ref. [6, Section 7]. We can use the average fidelity to define the average infidelity

$$\mu_{\mathrm{IF}_{\mathrm{avg}}} = 1 - \mu_{\mathrm{F}_{\mathrm{avg}}}.\tag{25}$$

In order to define a leakage measure for our NIGQCs, we make use of the second term in the numerator of Eq. (24). We define the leakage measure as

$$\mu_{\text{Leak}} = 1 - \left(\frac{\text{Tr}(\hat{M}\hat{M}^{\dagger})}{D}\right),$$
 (26)

where  $\operatorname{Tr}(\hat{M}\hat{M}^{\dagger})$  can be expressed as the sum of probability amplitudes. Hence, we find  $0 \leq \operatorname{Tr}(\hat{M}\hat{M}^{\dagger}) \leq D$ , and therefore it follows  $\mu_{\operatorname{Leak}} \in [0,1]$ .

The second error metric we consider is the diamond distance

$$\mu_{\diamond} = \frac{1}{2} \| \check{\mathcal{E}}_{\mathcal{M}} \check{\mathcal{E}}_{\mathcal{U}}^{-1} - \hat{I} \|_{\diamond}, \tag{27}$$

where  $\|\cdot\|_{\diamond}$  denotes the diamond norm, see Refs. [7, 8]. We can express the diamond distance in terms of an infimum

$$\mu_{\diamond} = \frac{1}{2} \inf_{Q \in GL_{4}(\mathbb{C})} \left\{ \| \left( \hat{V}, \hat{I} \right) \hat{Q}^{-\dagger} \hat{Q}^{-1} \left( \hat{V}, \hat{I} \right)^{T} \|_{2}^{\frac{1}{2}} \right.$$

$$\left. \| \left( \hat{V}, -\hat{I} \right) \hat{Q}^{\dagger} \hat{Q}^{1} \left( \hat{V}, -\hat{I} \right)^{T} \|_{2}^{\frac{1}{2}} \right\},$$

$$(28)$$

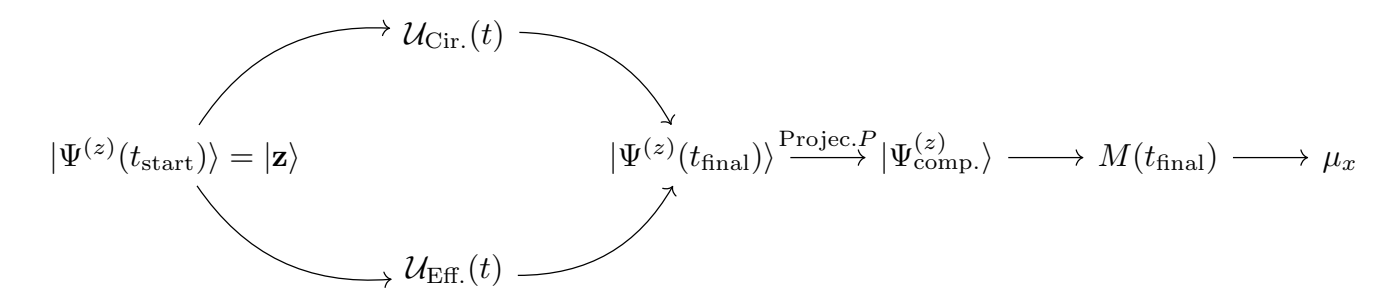


FIG. 3. Illustration of the computational process we use to obtain the gate-error quantifiers  $\mu_x$ . Here x is a label for an arbitrary metric and  $\hat{\mathcal{U}}_{\text{Cir.}}$  ( $\hat{\mathcal{U}}_{\text{Eff.}}$ ) is the time-evolution operator in Eq. (21) for the circuit (effective) Hamiltonian given by Eq. (2) (Eq. (7)). We compute the state vectors  $|\Psi^{(z)}(t_{\text{final}})\rangle$  with a product-formula algorithm, see Refs. [19, 20], for all computational basis states  $2^N$  of a NIGQC and then store the data in the matrix  $M(t_{\text{final}})$ . In this matrix, every column corresponds to the evolution of one computational state  $|\Psi^{(z)}_{\text{comp.}}\rangle = P|\Psi^{(z)}(t_{\text{final}})\rangle$ , where P denotes a projection matrix onto the computational subspace. We use the Message Passing Interface (MPI) to parallelise the  $2^N$  independent tasks. The computations are performed on the supercomputer JUWELS, see Ref. [30]. Finally, we compute the metric  $\mu_x$  with regard to a target operation U. The metrics we compute provide a measure for how close M and U are.

over all complex, invertible, two by two matrices, see Ref. [31]. Similarly, we can express the diamond distance in terms of a supremum

$$\mu_{\diamond} = \frac{1}{2} \sup_{|\psi\rangle \in \mathcal{H}^{2^{N}}} \left\{ \| \left( \hat{V}^{\dagger} \otimes \hat{I} \right) |\psi\rangle\langle\psi| \left( \hat{V}^{\dagger} \otimes \hat{I} \right)^{\dagger} - |\psi\rangle\langle\psi| \|_{T_{\Gamma}} \right\}, \tag{29}$$

over all state vectors of the Hilbert space of the IGQC, see Ref. [2]. We obtain the diamond distance up to the fourth decimal by cornering

$$\mu_{\diamond}^{(\inf)} \le \mu_{\diamond} \le \mu_{\diamond}^{(\sup)},$$
 (30)

the value  $\mu_{\diamond}$  with the infimum  $\mu_{\diamond}^{(\inf)}$  and supremum  $\mu_{\diamond}^{(\sup)}$  expressions in Eqs. (28) and (29). The algorithms we use are discussed in Ref. [29, Section 6.1.2].

Figure 3 illustrates the computational process we use to obtain the matrix M and in turn the various gate-error quantifiers  $\mu_x$  in this work. The label x denotes an arbitrary metric or measure. First, we simulate the time evolution  $|\Psi^{(z)}(t_{final})\rangle$  of the system for all  $2^N$  basis states  $|\Psi^{(z)}(t_{start})\rangle = |\mathbf{z}\rangle$  of the NIGQC. Note that we simulate the  $2^N$  time evolutions  $|\Psi^{(z)}(t)\rangle$  in parallel on the supercomputer JUWELS, see Ref. [30]. Then we make use of a projection matrix P and map the state vectors to the computational states  $|\Psi^{(z)}_{\text{comp.}}\rangle = P |\Psi^{(z)}(t_{final})\rangle$ . Finally, we store the data by building the matrix

$$M = \sum_{\mathbf{z} \in \{0,1\}^N} |\Psi_{\text{comp.}}^{(z)} \rangle \langle \mathbf{z}|, \qquad (31)$$

where  $|\mathbf{z}\rangle$  are the cartesian unit vectors, in the computer program. Finally, we compute the gate-error quantifiers  $\mu_x$  by means of the matrix  $V = UM^{\dagger}$ .

#### IV. RESULTS

In this section we present our findings. First, in Sec. IVA we discuss the spectrum of the four-qubit NIGQC illustrated in Figs. 1(c) and its relevance for the gate-error metrics we compute. Here we model the system with the circuit Hamiltonian Eq. (2). Next, in Sec. IVB we discuss the results of the calibration process for the different NIGQCs illustrated in Figs. 1(a-c). Here we consider both the circuit and the effective model. Then, in Sec. IV C we show how modelling the time evolution of NIGQCs with more and less basis states affects the gate-error quantifiers. Here we use the circuit Hamiltonian Eq. (2) to model the dynamics of the four-qubit NIGQC illustrated in Figs. 1(c). Next, in Sec. IV D we show how small deviations in a single control pulse parameter can affect gate-error metrics. Here we use the circuit Hamiltonian Eq. (2) to model the dynamics of the two-qubit, three-qubit and four-qubit NIGQCs illustrated in Figs. 1(a-c). Finally, in Sec. IV E we show how the commonly used adiabatic approximation for fluxtunable transmons affects gate-error metrics. Here we use the adiabatic and nonadiabatic effective Hamiltonian Eq. (2) to model the dynamics of the two-qubit, threequbit and four-qubit NIGQCs illustrated in Figs. 1(a-c).

#### A. Spectrum for a four-qubit NIGQC

In this section we discuss the spectrum of the fourqubit NIGQC illustrated in Fig. 1(c) and its relevance for the implementation of two-qubit gates.

Broadly speaking, the general idea of implementing two-qubit CZ gates with a UMP or BMP is to tune a target computational state like  $|0,0,1,1\rangle$  into resonance with a non-computational state like  $|0,0,0,2\rangle$ , wait some time until the population returns to the computational target state, and hope that this state has gained an ad-

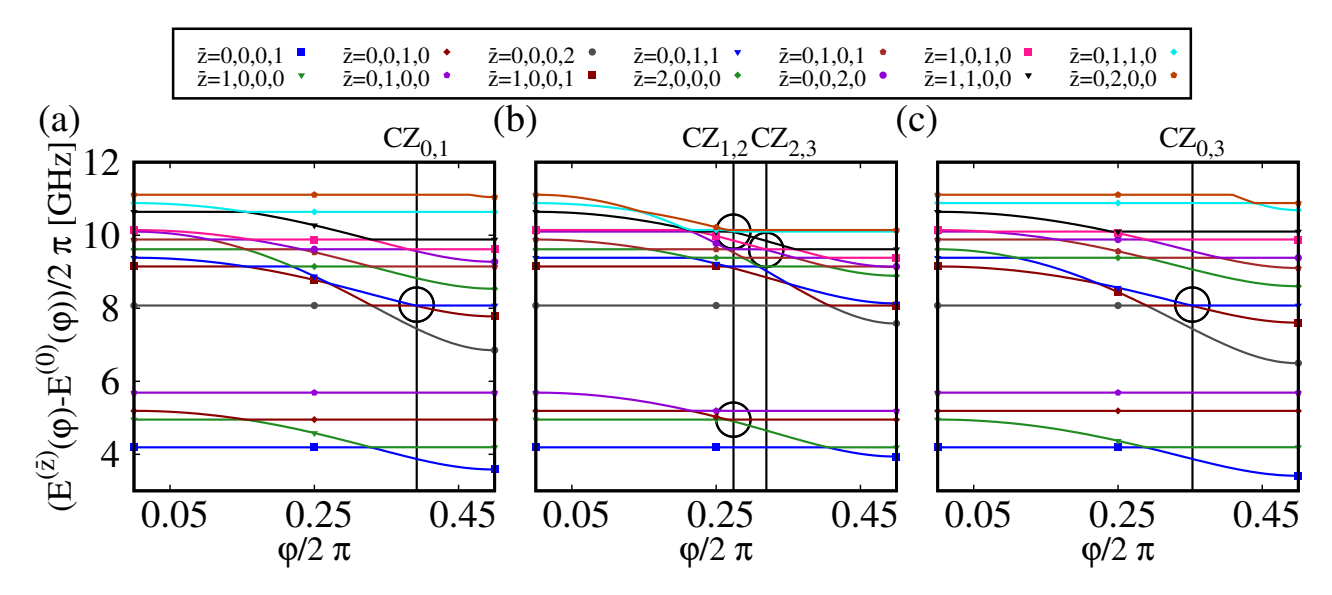


FIG. 4. (Color Online) The lowest fourteen energy levels of the four-qubit NIGQC illustrated in Fig. 1(c) as functions of the external flux offset  $\varphi$  for the second (i=1) in (a), the third (i=2) and the fourth (i=3) transmon qubit. We use the **circuit Hamiltonian** Eq. (2) and the device parameters listed in Table I to obtain the results with a standard diagonalisation algorithm, see Ref. [32]. All transmons are modelled with three basis states and all resonators are modelled with two basis states. We also mark (vertical lines) the pulse amplitudes  $\delta$  used to implement the CZ gates on the four-qubit NIGQC. Furthermore, we mark important energy level repulsions (ELRs) by means of black circles. In (b) we can observe that the pulse amplitude for the CZ<sub>1,2</sub> gate is near two ELRs. The first one is in the energy band between 4 and 6 GHz. This ELR leads to unwanted transitions between the first excited states of two qubits. The second one is in the energy band between 9 and 11 GHz. This ELR is used to implement the CZ<sub>1,2</sub> gate. In (a-c) we can observe that the other CZ gates do not suffer from the same problem. Furthermore, we can observe that driving different transmons (i=1) in (a), (i=2) in (b) and (i=3) in (c) leads to different spectral patterns.

ditional phase of  $e^{i\pi}$  with respect to all the other computational states of the NIGQC. The word "tune" in this context refers to tuning the energies of the instantaneous eigenstates of the system, i.e. the discussion is implicitly carried out in the instantaneous basis of the system. Additionally, single-qubit z-axis rotations  $R_i^{(z)}(\phi_i)$  are used to improve the performance, see Ref. [28, Section VII B 2].

The time it takes for our devices to swap the population back and forth between a computational and a non-computational state of the NIGQC lies between 75 and 100 ns. This time corresponds to the plateau time in Figs. 2(b-c). We fix these times by choosing the interaction strength constant G such that we approximately obtain the same gate times as in the experiment. Furthermore, the pulse amplitude  $\delta$  or the plateau height is fixed by the condition that the states involved in this process should have close-by energies. The time it takes to reach the plateau is crucial; we discuss this part of the gate implementation later in this section.

In Ref. [28, Section VII B 2], the authors differentiate between gates that are implemented adiabatically, see Ref. [33] and gates that are implemented nonadiabatically, see Ref. [34]. However, in the context of quantum theory the words adiabatic and nonadiabatic are usually associated with the adiabatic approximation, see Ref. [35, Section 6.6]. Note that the process described

above is clearly not an adiabatic one, i.e. the probability amplitudes of the state vector change over time. This and the fact that in almost all studies, the transmon qubit is modelled as an adiabatic anharmonic oscillator or as an adiabatic two-level system, leads us to the conclusion that in the context of the gate implementation protocol described above the words adiabatic and nonadiabatic are simply used to differentiate between gates with short and long pulse durations. Note that in Sec. IV E we investigate a related issue. There are two additional problems with the picture described above. First, assigning labels to the energies  $E_z(\varphi)$  and eigenstates  $|\phi_z(\varphi)\rangle$  of a continuous set of Hermitian matrices  $\{H(\varphi)\}\$ , where  $z \in \mathbb{N}^0$  and  $\varphi/2\pi \in [0,1]$ , is a non-trivial problem in itself, see Refs. [36-39]. Second, once we apply a UMP or BMP flux drive, we cannot guarantee that only the desired transitions occur.

In order to provide clarity on these issues, in the discussion of the four-qubit NIGQC spectrum, we do not adopt the same nomenclature used in Ref. [28, Section VII B 2].

Figures 4(a-c) show the lowest fourteen energy levels of the four-qubit NIGQC illustrated in Fig. 1(c) as functions of the external flux offset  $\varphi$  for the second (i=1) in (a), the third (i=2) and the fourth (i=3) transmon qubit. This means that each panel is obtained by repeatedly diagonalising the matrix for different flux offset

values  $\varphi/2\pi \in [0,0.5]$ . The results are obtained with the circuit Hamiltonian Eq. (2), the device parameters listed in Table I and a standard diagonalisation algorithm, see Ref. [32]. Here we use two basis states for the coupling resonators and three basis states for the different transmon qubits in the system. Note that the circuit Hamiltonian Eq. (4) has two symmetry points, one at  $\varphi/2\pi = 0.5$  and one at  $\varphi/2\pi = 1$ .

We label the energies  $E_{\bar{z}}$  of the interacting system according to the sorted energies  $E_z$  of the non-interacting system for the flux offset  $\varphi=0$ . The markers in Figs. 4(a-c) are there to guide the eye. Additionally, we employ black vertical lines to mark the flux offset values  $\varphi$  that correspond to pulse amplitudes  $\delta$  for the CZ gates in Table XIII. Furthermore, we employ black circles to mark the energy level repulsions (ELRs) that we use to implement the CZ gates and the ELRs that are problematic for the implementation of CZ gates with low gate-error metrics, see the line with two circles in Figs. 4(b).

If we start at the flux offset value  $\varphi = 0$  and then move to a value  $\varphi = \delta$  by driving a transmon qubit, we usually pass through several unused ELRs, i.e. not used to implement the CZ gates, with some of the computational basis states of the NIGQC before we reach the ELR or the flux offset value that we use to implement the CZ gate. Here we have to pass through the unused ELRs sufficiently fast because otherwise we can observe population exchange between the two states involved. This can be clearly observed (data not shown) if one studies the matrix in Eq. (31) while optimising the control pulse parameters or the probability amplitudes themselves during the time evolution of the system. Furthermore, one cannot move the system too fast, otherwise one observes (data not shown) all sorts of other transitions, e.g. the excited coupler states suddenly become populated. The pulse optimisation algorithm that we employ finds a balance between these two mechanisms and fine tunes the pulse amplitude  $\delta$  and the remaining pulse parameters such that nearly perfect population exchange occurs and the phases are aligned properly. Note that we have to take all  $2^N$  computational basis states into account, see Fig. 3.

In Fig. 4(b), we can also identify a problem that the optimisation cannot solve on its own, see the line with two circles. The ELR in the energy band between 4 GHz and 6 GHz induces a population exchange between two computational states of the NIGQC and is therefore unwanted. Furthermore, in the energy band between 9 GHz and 12 GHz for the same flux offset value, we can observe a dense structure of energy levels with many nearby ELRs.

Obviously, this leads to the question whether or not such a gate implementation scheme can be scaled up. To the best our knowledge, the largest PGQC to date with the device architecture discussed in this work has seventeen qubits, see Ref. [40]. In order to avoid the problem just discussed, i.e. frequency collisions during the gate, some authors suggest to apply additional flux pules to

non-interacting transmon qubits to mitigate the problem, see Ref. [16, Supplementary Material Section 1]. Other authors mitigate the issue by redefining the target two-qubit gate, see Ref. [41, Supplementary Material Section VI C 1], so that the time evolution of the system fits more naturally to the target two-qubit gate.

We emphasise that driving different transmon qubits results in different energy levels being populated and different ELRs being active, see Figs. 4(a-c). Consequently, before we can even start building a device, we have to solve an optimisation problem of exponential size, i.e. we have to avoid ELRs between all the  $2^N$  computational basis states of the NIGQC or PGQC. Note that here we have to take into account different pulse amplitudes  $\delta$  for the different CZ gates we implement and the different spectra and ELRs which result from driving different transmon qubits. Strictly speaking, our conclusions only apply to the frequency-tunable transmon device architecture studied in this work. However, the consequences of the problem are much more general and are imprinted on many other systems (cf. Ref. [42, 43]).

We also emphasise that using microwave pulses (MPs) to implement single-qubit gates leads to a similar problem, i.e. the MPs are not monochromatic and contain frequency components that can cause unwanted transitions. The more transmon qubits we employ, the more frequency components we have to take into account. If we consider an N-qubit transmon computer, we have to take into account that there are  $2^N$  relevant energy levels and the associated energy differences between these states. Each additional energy difference, i.e. transition frequency, reduces the available frequencies and thus adds to the frequency crowding problem (cf. Ref. [44]).

### B. Gate metrics for the elementary gate set

In this section we discuss the results of the control pulse optimisation procedure for the three different NIGQCs illustrated in Figs. 1(a-c).

Figures 5(a-d) show the diamond distance  $\mu_{\diamond}(a,b)$  and the average infidelity  $\mu_{\mathrm{IF}_{\mathrm{avg}}}(c,d)$  for the two-qubit (in blue), the three-qubit (in green) and the four-qubit (in red) NIGQCS modelled with the circuit Hamiltonian Eq. (2)(a,c) and the effective Hamiltonian Eq. (7)(b,d). The results are also listed in Tables XX–XXV, see Appendix D. The single-qubit  $R^{(x)}(\pi/2)$  rotations are implemented with the MP in Eq. (12). The two-qubit CZ gates are implemented with the UMP in Eq. (13). We use the device parameters listed in Table I and the pulse parameters listed in Tables VIII–XIX to obtain the results, see Appendix D. We employ the algorithms in the open-source Nlopt library, see Ref. [45], to perform the optimisation of the control pulse parameters.

The smallest values for the distance  $\mu_{\diamond}$  and the average infidelity  $\mu_{\rm IF_{avg}}$  obtained with the circuit Hamiltonian Eq. (2)(effective Hamiltonian Eq. (7)) are  $\mu_{\diamond} = 0.0080$  and  $\mu_{\rm IF_{avg}} = 0.0004$  ( $\mu_{\diamond} = 0.0089$  and  $\mu_{\rm IF_{avg}} = 0.0004$ )

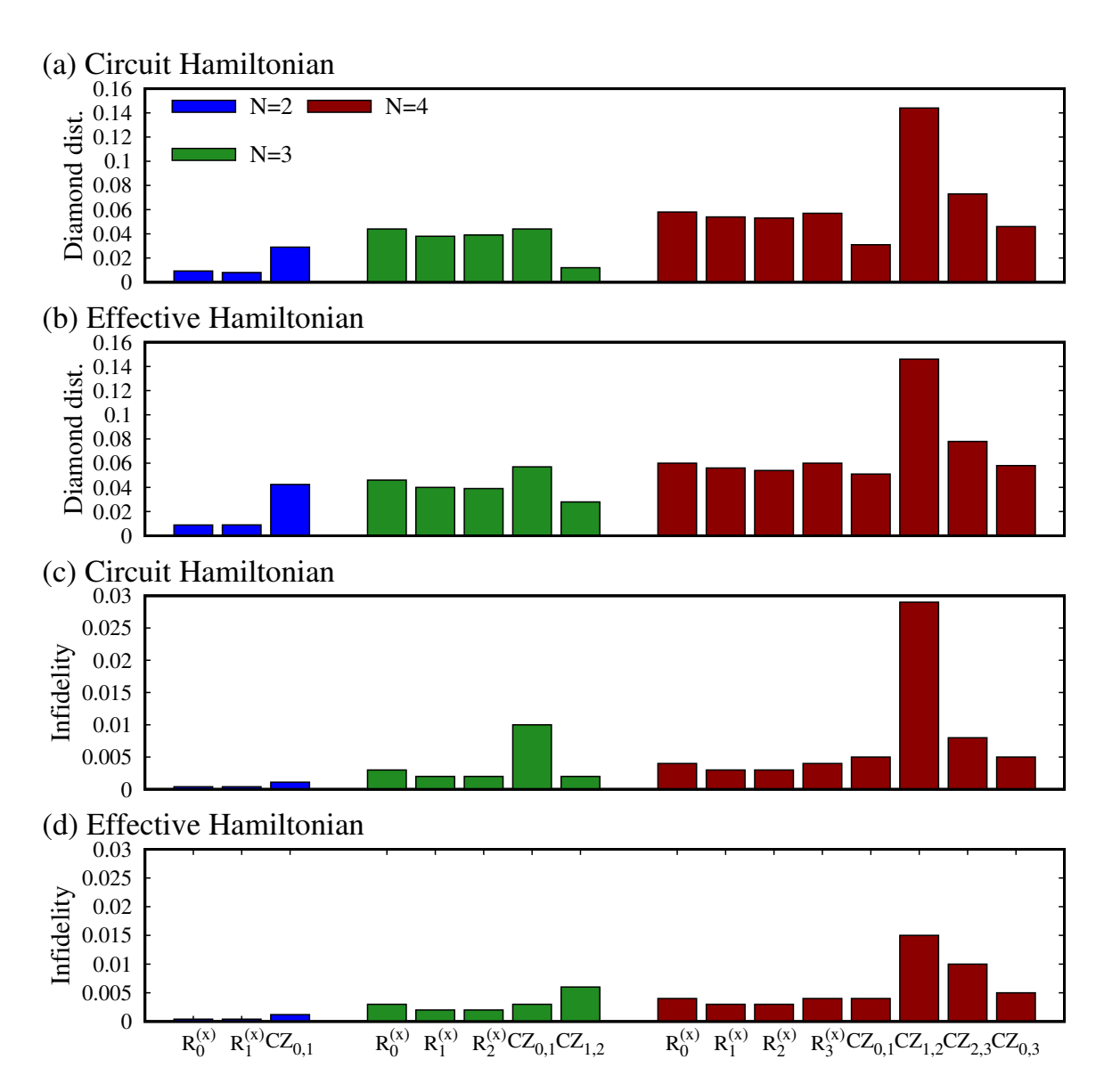


FIG. 5. (Color Online) Diamond distances  $\mu_{\diamond}(a,b)$  given by Eqs. (28) and (29) and average infidelity  $\mu_{\rm IF_{avg}}(c,d)$  given by Eq. (24) for  $R^{(x)}(\pi/2)$  rotations and CZ gates for the NIGQCs illustrated in Figs. 1(a-c), where N=2 in Fig. 1(a), N=3 in Fig. 1(b) and N=4 in Fig. 1(c). The error metrics are obtained with the **circuit Hamiltonian** Eq. (2) (a,c) and the **effective Hamiltonian** Eq. (7)(b,d). We use the device parameters listed in Table I and the pulse parameters listed in Tables VIII–XIX to obtain the results. The single-qubit  $R^{(x)}(\pi/2)$  rotations are obtained with a microwave pulse, see Fig. 2(a). The two-qubit CZ gates are obtained with the unimodal pulse, see Fig. 2(b).

for the  $R_0^{(x)}(\pi/2)$  ( $R_0^{(x)}(\pi/2)$ ) gate and the two-qubit NIGQC. Note that the same gate modelled with the circuit Hamiltonian Eq. (2)(effective Hamiltonian Eq. (7)) on the four-qubit NIGQC yields  $\mu_{\diamond} = 0.058$  and  $\mu_{\rm IF_{avg}} = 0.004$  ( $\mu_{\diamond} = 0.060$  and  $\mu_{\rm IF_{avg}} = 0.004$ ). Consequently, we have lost about one order of magnitude in accuracy by adding additional circuit elements to the system.

The largest values for the distance  $\mu_{\diamond}$  and the average infidelity  $\mu_{\rm IF_{avg}}$  obtained with the circuit Hamiltonian Eq. (2)(effective Hamiltonian Eq. (7)) are  $\mu_{\diamond} = 0.144$  and  $\mu_{\rm IF_{avg}} = 0.029$  ( $\mu_{\diamond} = 0.146$  and  $\mu_{\rm IF_{avg}} = 0.015$ ) for the CZ<sub>1,2</sub> gate and the four-qubit NIGQC.

We can potentially explain the large values for the  ${\rm CZ}_{1,2}$  gate-error metrics in both models by means of the energy level repulsions (ELRs) in Figs. 4(b). The ELR used to implement the  ${\rm CZ}_{1,2}$  gate is too close to other ELRs which lead to additional transitions between the states of the system. The optimisation algorithm cannot solve this problem. Note that we employ the quite accurate (see Ref. [25] and Ref. [18, Appendix B]) series expansions in Eqs. (B4) and (B7) to model the tunable qubit frequency and anharmonicity, respectively. If we employ the less precise first-order expansions, we cannot reproduce the results for the  ${\rm CZ}_{1,2}$  gate with the effective

model.

Furthermore, in Figs. 5(a-d) we can clearly observe a trend to larger gate-error metrics for larger systems, this is the case for both models. Note that the smallest system contains three circuit elements and the largest system consists of eight circuit elements.

While optimising the control pulse parameters for the two-qubit gates, we noticed that with increasing system size, i.e. the number of transmon qubits and couplers, it becomes more difficult to pass though the various ELRs in the spectrum sufficiently fast (slowly), see Figs. 4(a-c). If we let the pulse flanks, see Fig. 2(b), rise (fall) too slowly, we pass though various ELRs so slowly that unwanted population exchanges occur. If we let the pulse flanks rise (fall) too fast, we observe what are probably nonadiabatic transitions which can even excite the resonators. Obviously, there exists an analogous problem for drive frequencies  $\omega^{(D)}$  of the single-qubit  $R^{(x)}(\pi/2)$  rotations since the MP pulses are not strictly monochromatic. Both these problems can potentially explain the tendency to larger gate-error metrics in larger NIGQCs.

Furthermore, we also need to consider the difficult task given to the optimisation algorithm. Optimising the control pulse parameters for an N-qubit NIGQC amounts to aligning the time evolution of the system such that the matrix M given by Eq. (31) with  $2^{2N+1}$  double precision numbers is quasi perfectly aligned with the target matrix U. We do not know of an optimisation algorithm that can solve such a task with guarantee of success.

We also find (data not shown) that we cannot simply use the same optimised control pulse parameters for both the circuit model and the effective model. If we use the parameters of the circuit model for the effective model, we can observe diamond distances and average infidelities close to one. The reason for this is that parameters like the drive frequency  $\omega^{(D)}$  ( $\hbar\omega^{(D)}$ ) of the MP pulse and the pulse amplitude  $\delta$  ( $\hbar\omega^{(q)}(\delta)$ ) of the UMP must be at least fine tuned up to the sixth decimal (a couple of kHz). Also, the values that the optimisation algorithm obtains are very sensitive to changes in the model and the model parameters. For example, if the interaction strength G is changed from 300 MHz to 301 MHz, we would already need to restart the whole optimisation of the control pulse parameters to obtain gate-error metrics that are not significantly worse than the ones shown in Figs. 5(a-d). Obviously, this lack of robustness can be expected to become even more severe when an actual experiment, instead of a simulation, is conducted.

### C. Influence of higher states on gate-error trajectories obtained with the circuit Hamiltonian

In this section, we discuss simulation results for the implementation of  $R_0^{(x)}(\pi/2)$  gates on the four-qubit NIGQC illustrated in Figs. 1(c), modelled with the circuit Hamiltonian Eq. (2) using four and sixteen basis states for the transmon qubits. All resonators are mod-

TABLE II. Error metrics for a four-qubit NIGQC as illustrated in Fig. 1(c). The error metrics are obtained with the **circuit Hamiltonian** Eq. (7), the device parameters listed in Table I and the pulse parameters listed in Table XII. First column: target gate; second column: number of basis states used to model the dynamics of the transmons; third column: diamond distance  $\mu_{\diamond}$  given by Eqs. (28) and (29); fourth column: average infidelity  $\mu_{\rm IF_{avg}}$  given by Eq. (24); fifth column: leakage measure  $\mu_{\rm Leak}$  given by Eq. (26); sixth column: statistical distance given by Eq. (17). The statistical distance is obtained for the ground state of the NIGQC.

Gate	States	$\mu_{\diamond}$	$\mu_{ m IF}_{ m avg}$	$\mu_{\mathrm{Leak}}$	$\mu_{\mathrm{SD}}$
$R_0^{(x)}(\pi/2)$	4	0.0505	0.0037	0.0024	0.0014
$R_0^{(x)}(\pi/2)$	16	0.0584	0.0040	0.0024	0.0014

elled with four basis states. Furthermore, we use a fixed set of control pulse parameters for all simulations, see Table XII row one in Appendix D.

In Table II we show the results for two different simulations. In the first (second) case, we simulate the  $R_0^{(x)}(\pi/2)$  gate with four (sixteen) basis states for all transmon qubits in the system.

On the one hand, we can observe that the diamond distance  $\mu_{\diamond}$  exhibits an increase in the third decimal. Similarly, the average infidelity  $\mu_{\mathrm{IF}_{\mathrm{avg}}}$  increases in the fourth decimal. On the other hand, we can see that the leakage measure  $\mu_{\mathrm{Leak}}$  and the statistical distance  $\mu_{\mathrm{SD}}$  (obtained for the NIGQC computational basis state  $|0,0,0,0\rangle$ ) are the same, up the fourth decimal. Note that the leakage measure  $\mu_{\mathrm{Leak}}$  and statistical distance  $\mu_{\mathrm{SD}}$  are computed from the squares of the state vector amplitudes only. Consequently, the phase of the system is neglected completely. This makes both these quantifiers less susceptible to changes in the number of basis states.

Figures 6(a-d) show the diamond distance  $\mu_{\diamond}(a)$ , the average infidelity  $\mu_{\mathrm{IF}_{\mathrm{avg}}}(b)$ , the leakage measure  $\mu_{\mathrm{Leak}}(c)$  and the statistical distance  $\mu_{\mathrm{SD}}(d)$  as functions of the number of consecutively executed  $R_0^{(x)}(\pi/2)$  gates. Furthermore, we obtain the blue line when all transmon qubits are modelled with four basis states only. The green line is obtained when all transmon qubits are modelled with sixteen basis states. The statistical distance  $\mu_{\mathrm{SD}}$  is obtained for the initial state  $|0,0,0,0\rangle$  of the NIGQC.

The diamond distance  $\mu_{\diamond}(a)$  and the average infidelity  $\mu_{\mathrm{IF}_{\mathrm{avg}}}(b)$  modelled with four (in blue) and sixteen (in green) basis states start to deviate after the execution of a couple of  $R_0^{(x)}(\pi/2)$  gates. Finally, after twenty  $R_0^{(x)}(\pi/2)$  gates we find that the diamond distance  $\mu_{\diamond}(a)$  and the average infidelity  $\mu_{\mathrm{IF}_{\mathrm{avg}}}(b)$  deviate by about 10% for both cases. We also observe, that the leakage measure  $\mu_{\mathrm{Leak}}$  and the statistical distance  $\mu_{\mathrm{SD}}$  are less affected by changing the number of basis states, i.e. both gate-error quantifiers are roughly the same up to the fourth decimal. Note that usually gates are modelled with two or three basis states only, see for example Refs. [9, 46–50].

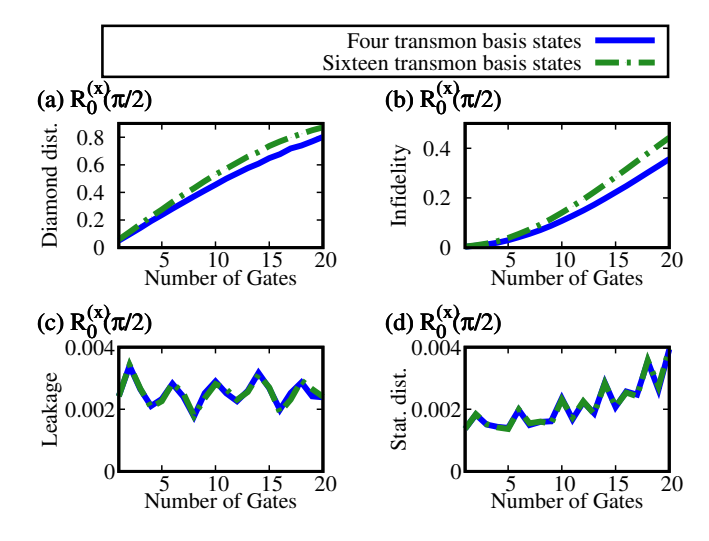


FIG. 6. (Color Online) Gate errors as functions of the number of gates for a program which executes twenty  $R^{(x)}(\pi/2)$ in a row. (a) diamond distance; (b) average infidelity; (c) leakage measure; (d) statistical distance for the initial state  $|0,0,0,0\rangle$ . We ran the gate sequence on the four-qubit NIGQC illustrated in Fig. 1(c). The results are obtained with the circuit Hamiltonian Eq. (2) and the device parameters listed in Table I. We ran the program twice. The first time with four basis states for every flux-tunable transmon in the system. These results are displayed with blue solid lines. The second time with sixteen basis states for every flux-tunable transmon in the system. These results are displayed with green dash-dotted lines. We observe that the gate-error metrics in (a-b) deviate by about 10% after twenty repetitions. The deviations for the gate-error metrics in (c-d) are smaller by more than a factor of one hundred.

Finally, we conclude that gate-error metrics obtained with a fixed number of basis states are only valid if the corresponding numerical values have actually converged. Changing the number of basis states can result in a new NIGQC model and there is no guarantee that the gateerror metrics obtained with the new model are the same as for the old model. Thereby we exclude the unlikely case that one can explicitly show that the truncated timeevolution operators, see Eqs. (21) and (31), for both models are the same. In practice, one has to increase the number of basis states until the results converge to a stable value that is independent of further increase. We followed this procedure for the results presented in this manuscript. Since in this section the intention was to highlight the relevance of this procedure, sometimes we did not follow it on purpose. Furthermore, the results presented in this section show that some gate-error metrics are less susceptible to changes in the number of basis states and that a growing number of gates might require us to use more basis states, to model the dynamics of the system.

TABLE III. Error metrics for a two-qubit NIGQC as illustrated in Figs. 1(a). The error metrics are obtained with the **circuit Hamiltonian** Eq. (7), the device parameters listed in Table I and the pulse parameters listed in Tables VIII and IX. First column: target gate; second column: offset value  $\Delta \delta$  we use to implement the CZ gates; third column: diamond distance  $\mu_{\diamond}$  given by Eqs. (28) and (29); fourth column: average infidelity  $\mu_{\text{IF}_{\text{AVg}}}$  given by Eq. (24); fifth column: leakage measure  $\mu_{\text{Leak}}$  given by Eq. (26); sixth column: statistical distance given by Eq. (17). The statistical distance is obtained for the ground states of the NIGQCs. We employ the UMP given by Eq. (13) to obtain the results.

Gate	$\Delta\delta/2\pi$	$\mu_{\diamond}$	$\mu_{ m IF}_{ m avg}$	$\mu_{ m Leak}$	$\mu_{\mathrm{SD}}$
$CNOT_{0,1}$	0	0.0386	0.0018	0.0012	0.0013
$\mathrm{CNOT}_{0,1}$	$10^{-6}$	0.0390	0.0018	0.0012	0.0013
$\mathrm{CNOT}_{0,1}$	$10^{-5}$	0.0456	0.0022	0.0012	0.0013
$\mathrm{CNOT}_{0,1}$	$10^{-4}$	0.1594	0.0156	0.0018	0.0038

### D. Influence of parameter changes on gate-error trajectories obtained with the circuit Hamiltonian

In this section we discuss simulation results for the implementation of  $CNOT_{0,1} = H_0CZ_{0,1}H_0$  gate repetition programs executed with the two-qubit, three-qubit and four-qubit NIGQCs illustrated in Figs. 1(a-c), modelled with the circuit Hamiltonian Eq. (2) and slightly different  $\delta + \Delta \delta$  control pulse parameters for the CZ<sub>0.1</sub> gates implemented with the UMP given by Eq. (13). In the following,  $\Delta \delta$  denotes the offset value. The original control pulse parameters for the UMPs we use to implement the  $CZ_{0,1}$  gates are listed in Table IX (Table XI, Table XIII) row one for the two-qubit (threequbit, four-qubit) NIGQC. All H<sub>0</sub> gates are implemented with  $R^{(x)}(\pi/2)$  rotations and virtual Z gates. We use the MP given by Eq. (12) and the control pulse parameters listed in Table VIII (Table X, Table XII) row one for the two-qubit (three-qubit, four-qubit) NIGQC. Note that for these simulations we do not optimise the circuit by eliminating the H<sub>0</sub> gates. We are interested in how the errors caused by different  $\Delta \delta$  interact with the single-qubit rotations. In this section, we model the dynamics of Hamiltonian Eq. (2) with sixteen basis states for all transmon qubits, except the one with the index i = 0, cf. Figs. 1(a-c), where we use four basis states. Additionally all resonators are modelled with four basis states only.

Table III shows the gate-error quantifiers for the execution of a single CNOT<sub>0,1</sub> on the two-qubit NIGQC illustrated in Figs. 1(a). The results are obtained with four slightly different pulse amplitudes  $\delta + \Delta \delta$  for the UMP which implements the CZ<sub>0,1</sub> gate. We use  $\Delta \delta/2\pi = 0$  in row one,  $\Delta \delta/2\pi = 10^{-6}$  in row two,  $\Delta \delta/2\pi = 10^{-5}$  in row three and  $\Delta \delta/2\pi = 10^{-4}$  in row four.

We observe that the diamond distance  $\mu_{\diamond}$  is affected by the third decimal if we change the pulse amplitude by  $\Delta \delta/2\pi = 10^{-6}$ . However, for this case the average

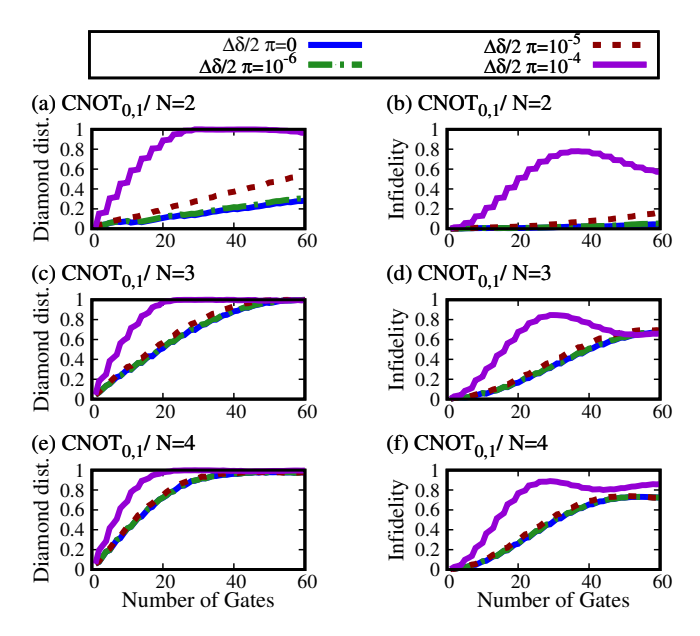


FIG. 7. (Color Online) Gate errors as functions of the number of gates for a program which executes twenty CNOT gates in a row. Note that every CNOT is implemented with one UMP pulse and two MP pulses. (a,c,e) diamond distance; (b,d,f) average infidelity. In (a,b) we run the program on the two-qubit NIGQC; in (c,d) we run the program on the three-qubit NIGQC and in (e,f) we run the program on the four-qubit NIGQC. The two-, three- and four-qubit systems are illustrated in Fig. 1(a-c), respectively. The results are obtained with the circuit Hamiltonian Eq. (2) and the device parameters listed in Table I. We run the program four times on each NIGQC. Each time we added an offset  $\Delta\delta$  to the pulse amplitude  $\delta$  of the UMP which implements the CZ gates. The results for the offset  $\Delta\delta/2\pi = 0$  ( $\Delta\delta/2\pi = 10^{-6}$ ).  $\Delta \delta/2\pi = 10^{-5}$ ,  $\Delta \delta/2\pi = 10^{-4}$ ) are shown in blue (green, red, violet) with solid (dashed, dashed, solid) lines. For the offset  $\Delta\delta/2\pi = 10^{-4}$  we can observe some type of tipping behaviour, i.e. the gate-error trajectory changes its form completely, see (a,b,d,f). Furthermore, we observe interesting non-linear behaviour for the gate-error trajectories which are generated by the CNOT sequence.

infidelity  $\mu_{\rm IF_{\rm avg}}$  is the same up to the fourth decimal. If we consider the offset value  $\Delta\delta/2\pi=10^{-5}~(\Delta\delta/2\pi=10^{-4})$ , we find that the diamond distance  $\mu_{\diamond}$  is affected by the second (first) decimal and the average infidelity  $\mu_{\rm IF_{\rm avg}}$  is affected by the third (second) decimal.

If we consider the flux-tunable qubit frequency of the transmon qubit we drive, see  $\omega_1^{(Q)}$  in Fig. 1(a), we find that keeping the pulse amplitude stable up to the sixth (fourth) decimal, for the offset  $\Delta\delta/2\pi=10^{-6}$ , means controlling the flux-tunable qubit frequency up to a couple of kHz (MHz). For this estimate of the energy scale we considered the spectrum of the corresponding circuit Hamiltonian with the device parameters listed in Table I row i=1.

Figures 7(a-f) show the diamond distance  $\mu_{\diamond}(a,c,e)$  and the infidelity  $\mu_{\rm IF_{avg}}(b,d,f)$  as functions of the number of gates for the two-qubit (a-b), three-qubit (c-d) and four-

qubit (e-f) NIGQCs illustrated in Figs. 1(a-c). Here we executed a gate sequence which contains twenty CNOT gates in a row on the different NIGQCs. In each panel we show the results for four different offsets;  $\Delta\delta/2\pi=0$  (blue solid),  $\Delta\delta/2\pi=10^{-6}$  (green dashed),  $\Delta\delta/2\pi=10^{-5}$  (red dashed) and  $\Delta\delta/2\pi=10^{-4}$  (violet solid). Note that each CNOT is implemented with two MPs and one UMP and we do not remove the H<sub>0</sub> gates from the circuit.

We observe that the qualitative and quantitative behaviour of the gate-error trajectories barely changes for the offset  $\Delta\delta/2\pi=10^{-6}$ , small deviations only become noticeable at the end of the repetition program. Once we increase the offset to  $\Delta\delta/2\pi=10^{-5}$ , we find that the qualitative and quantitative behaviour of the gate-error trajectories can be affected after a couple of gates. If we consider the offset to  $\Delta\delta/2\pi=10^{-4}$ , we can see some type of tipping behaviour in all panels, in the sense that the qualitative and quantitative behaviour of the gate-error trajectories can change in a non-linear manner. Note that one can obtain similar results by adding a frequency offset  $\Delta\omega^{(D)}$  to the drive frequency  $\omega^{(D)}$  of the single-qubit gate control pulse in Eq. (12).

Finally, we conclude that the stability of the gate-error metrics in our circuit Hamiltonian NIGQC model depends on our ability to control the flux-tunable qubit frequencies (the pulse amplitudes) up to a couple of kHz  $(\Delta\delta/2\pi=10^{-6}).$  Note that if we execute circuits which contain CZ gates, e.g. CZ<sub>0,1</sub>, CZ<sub>1,2</sub>, CZ<sub>2,3</sub> and CZ<sub>0,3</sub>, on different qubits and the corresponding UMPs are affected by the same offset  $\Delta\delta,$  then the system can become much more sensitive with regard to the offset value  $\Delta\delta,$  in comparison with the data, see Figs. 7(a-f) we discussed before.

We can convert the offset factor  $\Delta\delta/2\pi=10^{-6}$  for the flux  $\Delta\Phi=(\Phi_0\Delta\varphi)/2\pi$  from Weber to Tesla for an area of ten by ten micrometer which is characteristic for a flux-tunable transmon, see Ref. [51]. Using the circuit Hamiltonian Eq. (2) to simulate NIGQCs, we find that the gate-error metrics are sensitive to field strengths of about  $10^{-11}$  Tesla. Here we assume that the external flux is given by  $\Phi=|B|A$ , where |B| is the magnetic field strength and A is the area of the surface, where the flux is threading through. For comparison, the earth's magnetic field strength is about  $10^{-5}$  Tesla.

Furthermore, the data presented in this section suggests that, in our NIGQC model the gate-error metrics obtained for a single gate cannot be used to predict how the gate-error metrics behave in the future. Consequently, the future behaviour of a gate-error trajectory is not only determined by its initial value. We can explain this finding in very simple terms. The future state of the system  $|\Psi(t)\rangle$  is governed by the time-dependent Schrödinger equation given by Eq. (1) and not by the value of the gate-error metric  $\mu_x$  itself (x is a label for an arbitrary gate-error metrics. Therefore, there is no reason why gate-error metrics suffice to allow a prediction of the time evolution. They are at most a measure of closeness at one particular point in time, i.e. a snapshot

of the state of the system.

# E. Influence of the adiabatic approximation on gate-error trajectories obtained with the effective Hamiltonian

In this section we discuss simulation results for the implementation of  $CZ_{0,1}$  and  $CNOT_{0,1} = H_0CZ_{0,1}H_0$  gate repetition programs executed with the two-qubit, three-qubit and four-qubit NIGQCs illustrated in Figs. 1(a-c), modelled with the effective Hamiltonian Eq. (7) in the adiabatic and the nonadiabatic regime. In the adiabatic regime we set the time derivative  $\dot{\varphi}(t)$  of the external flux to zero such that the drive term in Eq. (10) is set to zero too. In the nonadiabatic regime, we do not make this assumption, i.e. we model the flux-tunable transmons as nonadiabatic anharmonic oscillators in the harmonic basis. For our simulations, we use four basis states for all transmons and resonators in the model.

For our simulations we employ the UMP, see Fig. 2(b), given by Eq. (13) and the BMP, see Fig. 2(c), given by Eq. (14) to test whether or not it is appropriate to model flux-tunable transmons in the adiabatic regime as it is commonly done in the literature, see e.g., Refs. [9, 28, 42, 46, 48–50, 52].

The results for the UMP (BMP) are presented in Table IV (Table V) and Figs. 8(a-l) (Figs. 9(a-l)). Note that the BMP in Fig. 2(c) shows a fast falling flank at around half of the pulse duration. Consequently, we expect that the deviations between the adiabatic and nonadiabatic case are larger for the BMP. Furthermore, the UMP and BMP are characterised by long time intervals of about 80 ns where the derivative  $\dot{\varphi}(t)$  of the external flux is zero in both models. Consequently, the deviations between the adiabatic and nonadiabatic model should originate from the pulse flanks we can see in Figs. 2(b-c).

The control pulse parameters for the UMPs and BMPs we use to implement the  $CZ_{0,1}$  gates are listed in Table XV (Table XVII, Table XIX) row one and two for the two-qubit (three-qubit, four-qubit) NIGQC. All  $H_0$  gates are implemented with  $R^{(x)}(\pi/2)$  rotations and virtual Z gates. We employ the MP given by Eq. (12) and the control pulse parameters listed in Table XIV (Table XVI, Table XVIII) row one for the two-qubit (three-qubit, four-qubit) NIGQC.

Table IV shows the gate-error quantifiers for the execution of a single  $CZ_{0,1}$  on the two-qubit (row one and two), three-qubit (row three and four) and four-qubit NIGQCs (row five and six) illustrated in Figs. 1(a-c). We implement the CZ gates with UMPs. The odd (even) row numbers show the results for the model in the adiabatic (nonadiabatic) regime. If we compare both cases for the different systems, we observe that the numerical values for the gate-error metrics and measure are nearly all the same except the ones for the diamond distance  $\mu_{\diamond}$ , we observe changes in the fourth and third decimal.

Figures 8(a-1) show the diamond distance

TABLE IV. Error metrics for a two-qubit, three-qubit and four-qubit NIGQC as illustrated in Figs. 1(a-c). The error metrics are obtained with the **effective Hamiltonian** Eq. (7), the device parameters listed in Table I and the pulse parameters listed in Tables XV, XVII and XIX. First column: target gate; second column: model we use to describe the flux-tunable transmons; i.e. the adiabatic or the nonadiabatic model; third column: diamond distance  $\mu_{\Diamond}$  given by Eqs. (28) and (29); fourth column: average infidelity  $\mu_{\mathrm{IF}_{\mathrm{avg}}}$  given by Eq. (24); fifth column: leakage measure  $\mu_{\mathrm{Leak}}$  given by Eq. (26); sixth column: statistical distance given by Eq. (17). The statistical distance is obtained for the ground states of the NIGQCs. Here we use the unimodal pulse (UMP) given by Eq. (13) to obtain the results.

Gate	Adiabatic	System	$\mu_{\diamond}$	$\mu_{ m IFavg}$	$\mu_{ m Leak}$	$\mu_{\mathrm{SD}}$
$CZ_{0,1}$	Yes	Figs. 1(a)	0.0424	0.0012	0.0005	0.0012
$CZ_{0,1}$	No	Figs. 1(a)	0.0425	0.0012	0.0005	0.0012
$CZ_{0,1}$	Yes	Figs. 1(b)	0.0569	0.0033	0.0017	0.0026
$CZ_{0,1}$	No	Figs. 1(b)	0.0574	0.0033	0.0017	0.0026
$\mathrm{CZ}_{0,1}$	Yes	Figs. 1(c)	0.0514	0.0040	0.0028	0.0025
$\operatorname{CZ}_{0,1}$	No	Figs. $1(c)$	0.0509	0.0040	0.0028	0.0025

 $\mu_{\circ}(a,e,i,c,g,k)$  and the average infidelity  $\mu_{\mathrm{IF}_{\mathrm{avg}}}(b,f,j,d,h,l)$  as functions of the number of gates for the two-qubit (a-d), three-qubit (e-h) and four-qubit (i-l) NIGQCs illustrated in Figs. 1(a-c). Here we executed programs which contain forty CZ(a,b,e,f,i,j) and forty CNOT(c,d,g,h,k,l) gates in a row on the different NIGQCs. As in Sec. IV D, we do not remove the  $\mathrm{H}_0$  gates from the circuit sequence to study how the errors of the CZ gates interact with the errors of the H gates. In each panel we show the results for the two different case; adiabatic regime (blue solid) and nonadiabatic regime (green dashed). Note that each CNOT is implemented with two MPs and one UMP this results in 120 gates in total.

If we consider Figs. 8(a-d) for the two-qubit NIGQC described by the effective Hamiltonian Eq. (7), we find that the small deviations between row one and two in Table IV can still affect the time evolution of the system such that the gate-error trajectories for the adiabatic and nonadiabatic model begin to diverge over time. Additionally, if we consider the results in Figs. 8(e-1) we also observe that the qualitative and quantitative behaviour of the gate-error trajectories can simply be affected by the presence of additional circuit elements. Note that we execute the same programs on NIGQCs of increasing size and that the device parameters in Table I for the first two transmon qubits and the coupling resonator do not change. However, each time we increase the size of the system we have to optimise the pulse parameters again. Therefore, if we consider the results presented in Sec. IVD, we expect a qualitative and quantitative change in the behaviour of the gate errors once we add additional circuit elements to the system and repeat the pulse optimisation. Furthermore, we observe that the

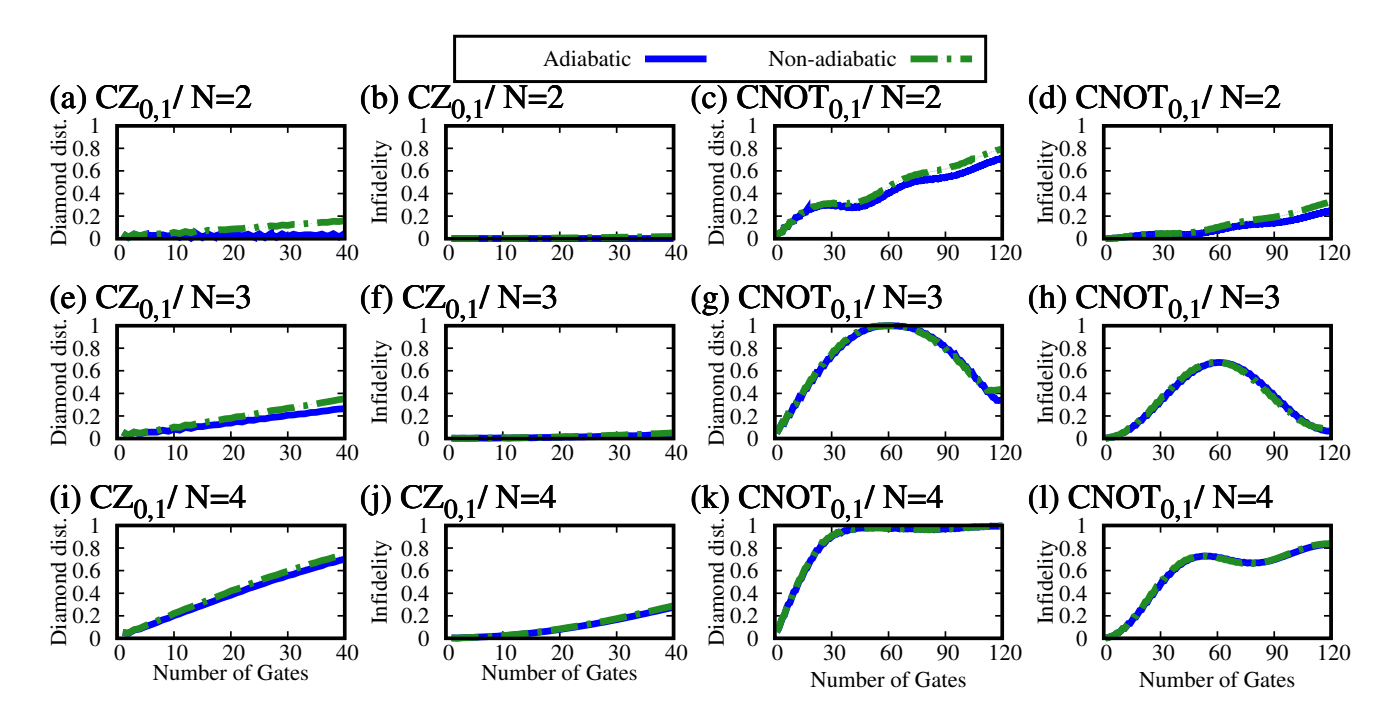


FIG. 8. (Color Online) Gate errors as functions of the number of gates for a program which executes forty CZ in a row, see (a,b,e,f,i,j) and a program which executes forty CNOT in a row, see (c,d,g,h,k,l). Note that every CNOT is implemented with one UMP pulse and two MP pulses. (a,c,e,g,i,k) diamond distance; (b,d,f,h,j,l) average infidelity. In (a-d) we run the program on the two-qubit NIGQC, in (e-h) we run the program on the three-qubit NIGQC and in (i-l) we run the program on the four-qubit NIGQC. The two-, three- and four-qubit systems are illustrated in Fig. 1(a-c), respectively. The results are obtained with the **effective Hamiltonian** Eq. (2) and the device parameters listed in Table I. We run the program two times on each NIGQC. On the first run, we model the flux-tunable transmons as adiabatic qubits. These results are displayed with blue solid lines. On the second run, we model the flux-tunable transmons as nonadiabatic qubits. These results are displayed with green solid lines. We can observe that the gate-error trajectories for the two cases can deviate up to 20% for the diamond distance and 10% for the average infidelity. Furthermore, we can observe a variety of interesting non-linear behaviour for the gate-error trajectories which are generated by the CNOT program.

gate-error trajectories for the CZ and CNOT programs show a substantially different qualitative and quantitative behaviour. Although, the deviations between the adiabatic and nonadiabatic case seem to be of the same order.

Overall, we find fair qualitative agreement for the adiabatic and nonadiabatic case. The UMPs we model in this work are quite long compared to instances which can be found in the literature, see for example Ref. [52]. Therefore, we emphasise that one cannot generalise the results presented in this section and argue that neglecting the nonadiabatic drive term in Eq. (10) is valid for all UMPs.

Table V shows the gate-error quantifiers for the execution of a single  $CZ_{0,1}$  on the two-qubit (row one and two), three-qubit (row three and four) and four-qubit NIGQCs (row five and six) illustrated in Figs. 1(a-c). We implement the CZ gates with BMPs. As before, the odd (even) row numbers show the results for the model in the adiabatic (nonadiabatic) regime. The even row number show the results for nonadiabatic regime. If we compare both cases for the different systems, we notice that the numerical values for the diamond distance  $\mu_{\diamond}$  show deviations

TABLE V. Error metrics for a two-qubit, three-qubit and four-qubit NIGQC as illustrated in Figs. 1(a-c). The error metrics are obtain with the **effective Hamiltonian** Eq. (7), the device parameters listed in Table I and the pulse parameters listed in Tables XV, XVII and XIX. The rows and columns show the same unit-less quantities as Table IV. Here we use the bimodal pulse (BMP) given by Eq. (14) to obtain the results.

Gate	Adiabatic	System	$\mu_{\diamond}$	$\mu_{ m IF}_{ m avg}$	$\mu_{ m Leak}$	$\mu_{ m SD}$
$\mathrm{CZ}_{0,1}$	Yes	Figs. 1(a)	0.0167	0.0006	0.0005	0.0004
$\mathrm{CZ}_{0,1}$	No	Figs. 1(a)	0.0195	0.0007	0.0005	0.0004
$\mathrm{CZ}_{0,1}$	Yes	Figs. 1(b)	0.0306	0.0042	0.0036	0.0020
$\mathrm{CZ}_{0,1}$	No	Figs. 1(b)	0.0336	0.0042	0.0035	0.0019
$\mathrm{CZ}_{0,1}$	Yes	Figs. $1(c)$	0.0415	0.0043	0.0035	0.0024
$CZ_{0,1}$	No	Figs. 1(c)	0.0435	0.0044	0.0035	0.0024

in the third decimal. Furthermore, the numerical values for some of the average infidelities  $\mu_{\rm IF_{avg}}$  show deviations in the fourth decimal. The leakage measure  $\mu_{\rm Leak}$  and the statistical distance  $\mu_{\rm SD}$  are only affected in one case, see row three and four.

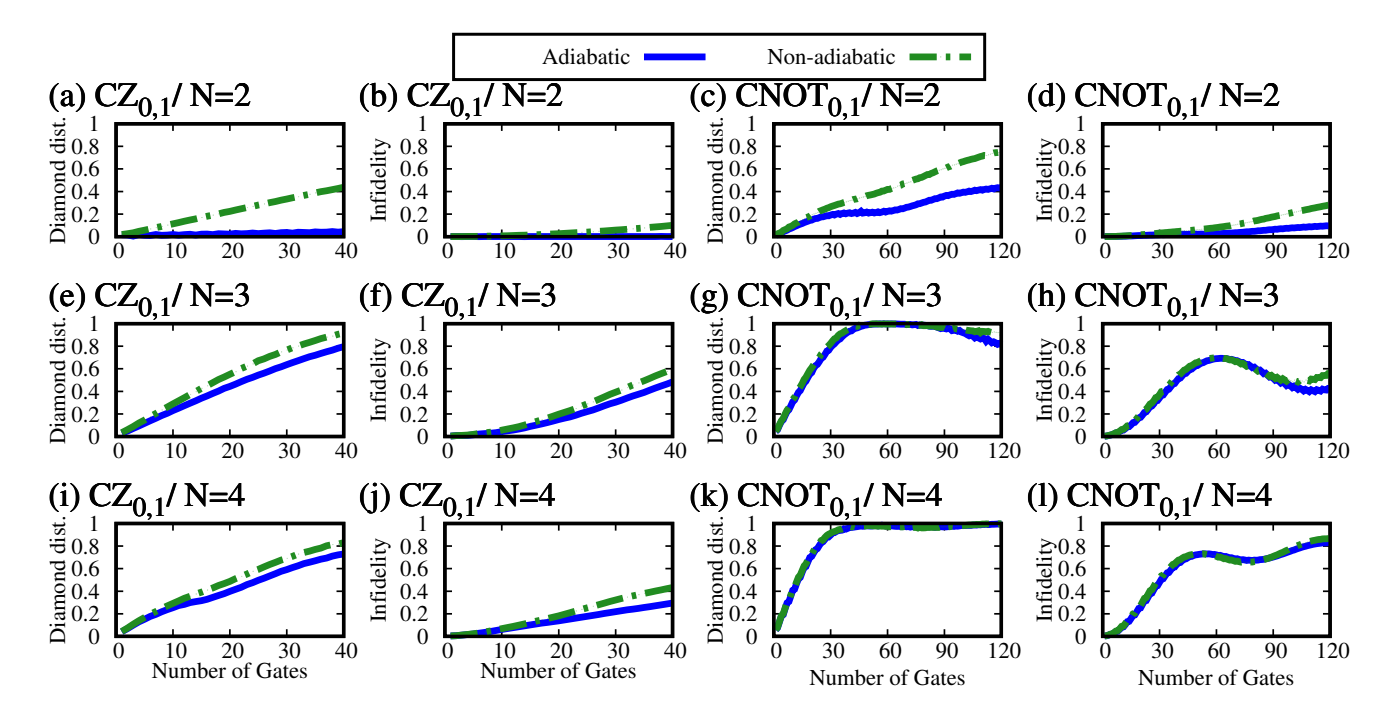


FIG. 9. (Color Online) Gate errors as functions of the number of gates for a program which executes forty CZ in a row, see (a,b,e,f,i,j) and a program which executes forty CNOT in a row, see (c,d,g,h,k,l). Note that every CNOT is implemented with one BMP pulse and two MP pulses. (a,c,e,g,i,k) diamond distance; (b,d,f,h,j,l) average infidelity. In (a-d) we run the program on the two-qubit NIGQC, in (e-h) we run the program on the three-qubit NIGQC and in (i-l) we run the program on the four-qubit NIGQC. The two-, three- and four-qubit systems are illustrated in Fig. 1(a-c), respectively. The results are obtained with the **effective Hamiltonian** Eq. (2) and the device parameters listed in Table I. We run the program two times on each NIGQC. On the first run, we model the flux-tunable transmons as adiabatic qubits. These results are displayed with blue solid lines. On the second run, we model the flux-tunable transmons as nonadiabatic qubits. These results are displayed with green dashed lines. We can observe large qualitative and quantitative deviations for the gate-error trajectories which are generated by the two different models. Furthermore, we observe a variety of interesting non-linear behaviour for the gate-error trajectories which are generated by the CZ and CNOT programs.

Figures 9(a-1) show the diamond distance  $\mu_{\diamond}(a,e,i,c,g,k)$  and the infidelity  $\mu_{\mathrm{IF}_{\mathrm{avg}}}(b,f,j,d,h,l)$  as functions of the number of gates for the two-qubit (a-d), three-qubit (e-h) and four-qubit (i-l) NIGQCs illustrated in Figs. 1(a-c). We executed programs which contain forty CZ(a,b,e,f,i,j) and forty CNOT(c,d,g,h,k,l) gates in a row on the different NIGQCs. As before, we do not remove the  $H_0$  gates from the circuit sequence to study how the errors of the CZ gates interact with the errors of the H gates. In each panel we show the results for the two different cases; adiabatic regime (blue solid) and nonadiabatic regime (green dashed).

In Figs. 9(a-l) we see that the small numerical deviations in the third and fourth decimal for the gate-error metrics listed in Table V can over time result in substantial changes in the qualitative and quantitative behaviour of the gate-error trajectories which result from modelling transmon qubits in the adiabatic regime. Furthermore, we find that overall the deviations between the adiabatic and nonadiabatic model are much larger than for the case where we implement the CZ gates with UMPs instead of BMPs. Note that the BMP and UMP in Figs. 2(b-c) are very similar except for the large pulse flank in the mid-

dle of the BMP pulse. If we compare Figs. 8(a-d) and Figs. 9(a-d), we also find that the qualitative and quantitative behaviour of the gate-error trajectories is not the same if we model them with different pulses. However, this is not surprising since in Sec. IV D we have already seen that gate-error trajectories are also very sensitive to changes in the model parameters and both sets of pulse parameters were optimised independently, i.e. this can potentially explain why we see these substantial differences.

We emphasise that we have selected data which highlights the small border between the adiabatic and nonadiabatic regime. In Appendix C, we show the results for a different device architecture which is discussed in Refs. [46, 48, 49, 53] for which the results obtained with the two different models deviate much stronger. Furthermore, the authors of Ref. [9] use an adiabatic effective model to describe a flux driven two-qubit system which consists of two transmon qubits and a coupling resonator. Here bimodal flux pulses with much shorter gate durations are considered. The data presented in this section suggests that the corresponding numerical results change once the flux drive term in Eq. (10) is part of the effec-

tive model. The reader may recall that in this section we only considered one approximation, i.e. assumption, which simplifies the model Hamiltonian. Most of the effective Hamiltonians used are the result of numerous approximations.

Finally, we conclude that it is not possible to decide beforehand whether or not an approximation, i.e. an assumption which affects the time evolution of the system. is justified when it comes to modelling gate-error metrics like the diamond distance or the average infidelity. As before, we exclude the unlikely case that we can explicitly show that the truncated time-evolution operators, see Eqs. (21) and (31), for both models are the same. Consequently, every approximation (assumption) constitutes a new NIGQC model and we do not know whether or not the old reference model yields the same gate-error metrics. The data discussed in this section leads to the conjecture that the quantitative and qualitative behaviour of gate-error trajectories is not simply given by the sum of the individual gate-errors but emerges due to a complex interplay of small deviations with respect to the target gates which occur over time (cf. Refs. [54–56]). Note that the Hamiltonians, see Eq. (7), for the adiabatic and nonadiabatic case only deviate for small periods of time and that the gate-errors for the different models gradually diverge over time and in the end might show a substantially different qualitative and quantitative behaviour.

Furthermore, as in Sec. IV D, the data presented in this section suggests that, in our NIGQC models the gate-error metrics obtained for a single gate cannot be used to predict how the gate-error metrics for the next gates in the gate sequence (the program) behave. Consequently, the future behaviour of a gate-error trajectory is not only determined by its initial value. As before, we can explain this finding as follows. The future state of the system  $|\Psi(t)\rangle$  is still governed by the time-dependent Schrödinger equation given by Eq. (1) and not the value of the gate-error metric itself. Consequently, there is no reason why gate-error metrics should allow a prediction of the time evolution of the system beforehand. Note that we can clearly observe a divergence between the two types of NIGQC models we studied in this section.

### V. SUMMARY, DISCUSSION AND CONCLUSION

We have studied the gate-error trajectories which arise if one repeats a gate several times in a row. For the simulations we modelled two-qubit, three-qubit and four-qubit superconducting non-ideal gate-based transmon quantum computers or non-ideal gate-based quantum computers (NIGQCs) for short, see Sec. I and Fig. 1(a-c). The time evolution of the state vector  $|\Psi(t)\rangle$  which by assumption completely determines the state of a NIGQC is generated by the time-dependent Schrödinger equation for a time-dependent Hamiltonian  $\hat{H}(t)$ . We used the circuit Hamiltonian Eq. (2) and the associated effective

Hamiltonian Eq. (7) to generate the dynamics of the systems. The control pulses discussed in Sec. II C were used to implement two types of gates. We used the microwave pulse (MP) in Eq. (12), see Fig. 2(a), to implement the single-qubit  $R^{(x)}(\pi/2)$  rotations. We also implemented CZ gates. We either use the unimodal pulse (UMP) in Eq. (13), see Fig. 2(b) or the bimodal pulse (BMP) in Eq. (14), see Fig. 2(c). This allowed us to compute various gate-error metrics like the diamond distance and the average infidelity as functions of the number of gates executed on the NIGQCs. For the computations we implemented the product-formula algorithms to solve the time-dependent Schrödinger equation, see Ref. [57, Section 4.1-4.8], the algorithms discussed in Ref. [58] to determine the state  $|\psi\rangle$  of the ideal gate-based quantum computer (IGBC) and the open-source library Nlopt, see Ref. [45], to optimise the control pulse parameters. The complete simulation software with exception of the optimisation algorithms was developed and implemented in house. The main results in this manuscript are presented in Sec. IV. All results in this work are obtained with the device parameters listed in Table I.

In Sec. IV A we discussed the spectrum of the fourqubit NIGQC illustrated in Fig. 1(c) and its relevance for the implementation of two-qubit CZ gates. We modelled the system with the circuit Hamiltonian Eq. (2) and discussed how the complexity of the energy levels which increases with the system size, i.e. the number of transmon qubits and couplers, can affect the gate-error metrics of the two-qubit CZ gates that we considered. Furthermore, this problem also affects the scaling-up capabilities of the device architecture discussed in this work.

In Sec. IVB we discussed the results of the control pulse optimisation, see Fig. 5 and Tables XX–XXV. The corresponding control pulse parameters are listed in Tables VIII–XIX in Appendix D. We found that the gateerror metrics have a tendency to grow with the system size and that we can explain this tendency by studying the energy spectrum of the system, see for example Fig. 4(a-c) and by assessing the difficult task we hand over to the optimisation algorithms that we need to use.

In Sec. IV C we studied a simple sequence which consists of twenty single-qubit  $R^{(x)}(\pi/2)$  gates on a fourqubit NIGQC, see Fig. 1(c). We modelled the system by the circuit Hamiltonian Eq. (2) and computed gateerror metrics with four and sixteen basis states for every flux-tunable transmon in the system. The results are displayed in Figs. 6(a-d). We found that after twenty repetitions the diamond distances and the average infidelities computed with different numbers of basis states deviate by about 10%. Furthermore, we also saw that the deviations for the leakage error measure and the statistical distances are smaller by about a factor of one hundred. This can potentially be explained by the fact that these gate-error quantifiers are computed from the squares of the state vector amplitudes only. Note that gates are often modelled with two or three basis states only, see for example Refs. [9, 46–50].

In Sec. IVD we studied a sequence which consists of twenty CNOT gates on a two-qubit, a three-qubit and a four-qubit NIGQC, see Figs. 1(a-c) respectively. The results are shown in Figs. 7(a-f). We modelled the system by the circuit Hamiltonian Eq. (2) and used the UMP given by Eq. (13), see Figs. 2(b), to implement the CZ gates. We repeated the simulations four times and added the offsets  $\Delta \delta / 2\pi \in \{0, 10^{-6}, 10^{-5}, 10^{-4}\}$  to the calibrated control pulse amplitudes  $\delta$  which implement the CZ gates. The parameters can be found in the first rows of Tables IX, XI and XI. We found that the gateerror metrics are affected, to some extent, by all three non-zero offset values  $\Delta \delta$ . We also noticed some type of tipping behaviour for the offset factor  $\Delta \delta/2\pi = 10^{-4}$ , i.e. the qualitative and qualitative behaviour of the gateerror trajectories changed drastically for this offset. This was the case for all three systems, see Figs. 1(a-c). If we convert the offset factor  $\Delta\delta/2\pi = 10^{-6}$  for the flux  $\Delta\Phi = (\Phi_0\Delta\varphi)/2\pi$  from Weber to Tesla for an area of ten by ten micrometer which is characteristic for a flux-tunable transmon, see Ref. [51], we find that the gate-error metrics in NIGQCs modelled with the circuit Hamiltonian Eq. (2) are sensitive to field strengths of about  $10^{-11}$  Tesla. For reasons of comparison, we state that the earth's magnetic field strength is about  $10^{-5}$ Tesla strong. Additionally, we found that the gate-error trajectories which are generated by the circuit Hamiltonian Eq. (2) and the time-dependent Schrödinger equation exhibit interesting non-linear behaviour.

In Sec. IVE we present results for sequences of forty CZ and forty CNOT gates on two-qubit, three-qubit and four-qubit NIGQCs. The results are shown in Figs. 8(a-1) and Figs. 9(a-1). We modelled the system with the effective Hamiltonian Eq. (7) and used the UMP to obtain the results in Figs. 8(a-1) and the bimodal pulse to to obtain the results in Figs. 9(a-1). We ran the CZ and CNOT sequences on two different types of NIGQCs. On the first type of NIGQC the flux-tunable transmons are modelled adiabatically, i.e. we set the time derivative  $\dot{\varphi}(t) = 0$ of the external flux, which is used to implement the CZ gates, to zero. On the second type of NIGQC we model all flux-tunable transmons non adiabatically. Although the UMP we used seemingly justifies the adiabatic approximation, see Fig. 2(b), we found that the results for the diamond distance can vary up to 0.2 and the results for the average fidelity up to 0.1. Furthermore, in most cases the qualitative behaviour of the gate-error trajectory is not affected by the adiabatic approximation for the UMP. The bimodal pulses we used do not seem to justify making the adiabatic approximation, see Fig. 2(c) and in fact we found that the corresponding gate-error trajectories for the adiabatic and nonadiabatic case show strong qualitative and quantitative deviations. Additionally, we also observed that the gate-error trajectories which are generated by the effective Hamiltonian Eq. (7) and the time-dependent Schrödinger equation show interesting non-linear behaviour. Furthermore, we found that the qualitative behaviour of the gate-error trajectories for the CZ and CNOT gates are usually not the same. In fact, often they show a completely different behaviour. Therefore, we suspect that the qualitative behaviour of a gate-error trajectory is not simply given by the sum of the individual errors but arises due to a complex interplay of small deviations with respect to the target gates.

The results in Secs. IV B–IV E show that even seemingly small changes in the model, i.e. in the assumptions we make, can substantially affected the gate-error metrics we compute. The fact itself is not surprising and something one should expect. However, the extent to which the changes affect the gate-error metrics during the course of the time evolution is something worth knowing. Note that in each section we focused on one aspect of the model which affects the computation of gate-error metrics. One can easily imagine what happens if one begins to combine changes in the different aspects of the models, namely that we cannot determine a root cause anymore.

Based on the data presented in Secs. IV A-IV E, we conclude that almost all assumptions we make about the model can substantially affect the time-evolution of the systems and consequently the gate-error metrics we model. Therefore, we advocate the view that every assumption leads to a new independent NIGQC model and we simply cannot estimate how the different assumptions affect the gate-error metrics we model. Again we exclude the unlikely case that we can explicitly show that the truncated time-evolution operators, see Eqs. (21) and (31), for both models are the same. Therefore, the data presented in this work emphasises the narrow borders between certain NIGQC models. Note that we could have selected other data which shows much larger deviations between the various NIGQC models. However, emphasising the narrow path between two seemingly very similar models also has the benefit of adding evidence to our conjecture that in NIGQC models gate errors for consecutive gates are not simply given by the sum of the gate errors for the individual gates in the program sequence but emerge due to a complex interplay of small deviations with respect to the target gates which occur over time (cf. Refs. [54–56]).

Since we found that nearby values for the diamond distance and the average infidelity for a given target gate can lead to very different qualitative behaviour for the gate-error trajectories which arise if we execute the target gate several times, we conclude that the gate-error metrics for a given target gate cannot be used to predict the behaviour of the gate-error sequence which emerges over time. Note that we showed this with two different generic model Hamiltonians Eqs. (2) and (7), i.e. this is not a feature of one particular model. Furthermore, if we take into account the results in Refs. [3, 29], we also find that this not a feature of one particular device architecture. Consequently, we advocate the view that gate-error metrics are at most snapshots for the state of a system at one particular moment in time and not predictors of the gate errors which emerge over time and/or the performance for complete programs (algorithms) executed

on the system. In fact, this shortcoming is something we should expect. The gate-error metrics we compute are derived in the context of the IGQC model. This model is inherently static, i.e. changes in the state of the system are modelled as if they occur instantaneously. However, if the future state of the system is governed by the time-dependent Schrödinger equation, there is no reason why gate-error metrics alone should be able to predict the time-evolution of the system. They are at most a measure of closeness at one particular point in time.

This then leads to the question: how can we actually study gate errors in PGQCs if, in most cases, we cannot conclusively compare two NIGQC models and determine where the differences in the gate-error metrics originate from? In Sec. I, we briefly mentioned, see Refs. [9–12, 59, 60], several problems which plague superconducting PGQCs. The seemingly more complex circuit Hamiltonian Eq. (2) is derived on the basis of the lumped-element approximation, see Ref. [17, Section 1.4 and neglects many of these problems by assumption. Additionally, it is not a trivial task to access the state vector and/or the density operator which is supposed to describes the complete state of a PGQC, also by assumption. Adding this uncertainty to all the other uncertain factors in an experiment, we find ourself in a position where studying individual gate errors in an actual experiment seems impossible. Therefore, we advocate the view that one should use benchmark protocols like the ones discussed in Refs. [3, 4] to assess and/or compare different PGQCs.

In this work we focused on the execution of simple gate sequences which generate interesting gate-error trajectories for various simulation settings. For future work, it might be interesting to see how variational hybrid algorithms like for example the quantum approximate optimization algorithm, see Refs. [61, 62], perform on the NIGQCs calibrated for this work.

#### ACKNOWLEDGMENTS

The authors gratefully acknowledge the Gauss Centre for Supercomputing e.V. (www.gauss-centre.eu) for funding this project by providing computing time on the GCS Supercomputer JUWELS [30] at Jülich Supercomputing Centre (JSC). H.L. acknowledges support from the project OpenSuperQ (820363) of the EU Quantum Flagship. D.W.'s work was partially supported by the Q(AI)<sup>2</sup> project. H.L., D.W. and M.W. acknowledge support from the project Jülich Unified Infrastructure for Quantum computing (JUNIQ) that has received funding from the German Federal Ministry of Education and Research (BMBF) and the Ministry of Culture and Science of the State of North Rhine-Westphalia.

### Appendix A: Derivation of a circuit Hamiltonian for flux-tunable transmons with an additional charge drive term

In the main text we use the circuit Hamiltonian Eq. (4) to model flux-tunable transmons with a linear charge drive term.

In this appendix, we derive circuit Hamiltonian Eq. (4) from the assumptions which constitute the lumpedelement approximation, see Ref. [17, Section 1.4]. The external charge variable  $n_g(t)$  provides us with a linear drive term which can be used to implement single-qubit gates. Similarly, the external flux variable  $\Phi_e(t)$  provides us with a drive term which can be used to implement two-qubit gates. The following derivation is motivated by the work in Ref. [23], i.e. we take into account recent developments in the theory of circuit quantisation. Note that the underlying assumptions we use are slightly different from the ones used in Ref. [23]. We use  $\hbar = 1$  throughout this work.

We begin with the quantisation of the lumped-element circuit illustrated in Fig. 10. Kirchhoff's voltage law yields

$$\Phi_l(t) + \Phi_r(t) = \Phi_e(t), \tag{A1}$$

for the central loop of the circuit. In our lumped-element model, we treat the external flux  $\Phi_e(t)$  as an electromotive force (EMF)  $\dot{\Phi}_e(t)$ .

We intend to express the Lagrangian  $\mathcal{L}$  of the system in terms of the variable

$$\Phi(t) = m_l \Phi_l(t) + m_r \Phi_r(t). \tag{A2}$$

Note that the left

$$\Phi_l(t) = \frac{(\Phi(t) - m_r \Phi_e(t))}{m_{\Delta}} \tag{A3}$$

and the right

$$\Phi_r(t) = -\frac{(\Phi(t) - m_l \Phi_e(t))}{m_{\Delta}}, \tag{A4}$$

branch flux variables satisfy Eq. (A1) for all  $m_l, m_r \in \mathbb{R}$  without further ado. Here  $m_{\Delta} = m_l - m_r$ .

If we make use of the relations  $V_{C_l} = V_{E_{J_l}}$  and  $V_{C_r} = V_{E_{J_r}}$  for the left and right loop in Fig. 10, we can express the Lagrangian as

$$\mathcal{L} = \frac{C_l}{2} \left( \frac{\left(\dot{\Phi}(t) - m_r \dot{\Phi}_e(t)\right)}{m_{\Delta}} \right)^2 + \frac{C_r}{2} \left( \frac{\left(\dot{\Phi}(t) - m_l \dot{\Phi}_e(t)\right)}{m_{\Delta}} \right)^2 - U\left(\Phi(t)\right),$$
(A5)

where the potential energy term  $U(\Phi(t))$  reads

$$U(\Phi(t)) = -E_{J_l} \cos\left(\frac{2\pi}{\Phi_0} \frac{(\Phi(t) - m_r \Phi_e(t))}{m_\Delta}\right) - E_{J_r} \cos\left(\frac{2\pi}{\Phi_0} \frac{(\Phi(t) - m_l \Phi_e(t))}{m_\Delta}\right).$$
(A6)

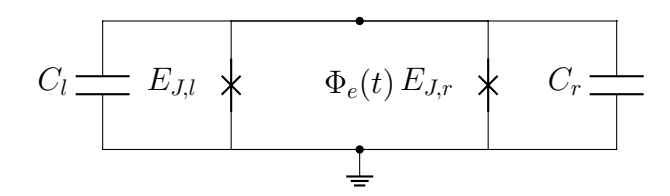


FIG. 10. Illustration of a lumped-element circuit with two linear capacitors with capacitances  $C_l$  (left) and  $C_r$  (right), two Josephson junctions with Josephson energies  $E_{J,l}$  (left) and  $E_{J,r}$  (right) and an external flux  $\Phi_e(t)$  threading through the central loop. As it is common practice, we mark the ground node by a dashed triangle.

In a next step, we evaluate the squares and neglect all factors proportional to  $\dot{\Phi}_e(t)^2$ , which ultimately only contribute non-measurable global phase factors to the time-evolution of the system. The Lagrangian after this step reads

$$\mathcal{L} = \frac{C_{\Sigma}}{2m_{\Delta}^2} \dot{\Phi}(t)^2 - \frac{(C_l m_r + C_r m_l)}{m_{\Delta}^2} \dot{\Phi}_e(t) \dot{\Phi}(t) - U\left(\Phi(t)\right). \tag{A7}$$

The conjugate variable

$$Q = \frac{C_{\Sigma}}{m_{\Delta}^2} \dot{\Phi}(t) - \frac{(C_l m_r + C_r m_l)}{m_{\Delta}^2} \dot{\Phi}_e(t), \tag{A8}$$

can be used to obtain the Hamiltonian function

$$H = \frac{m_{\Delta}^2}{2C_{\Sigma}} Q^2 + \frac{(C_l m_r + C_r m_l)}{C_{\Sigma}} \dot{\Phi}_e(t) Q + U(\Phi(t)), \text{ (A9)}$$

by means of a Legendre transformation, see Ref. [63]. Here again we neglect all factors which only contribute a non-measurable global phase factors to the time evolution of the system.

Finally, we can promote the conjugate variables  $\Phi$  and Q to the conjugate operators  $\hat{\Phi}$  and  $\hat{Q}$  and perform the substitutions

$$\hat{\varphi} = \frac{2\pi}{\Phi_0} \hat{\Phi},\tag{A10a}$$

$$\hat{n} = \frac{1}{2e}\hat{Q},\tag{A10b}$$

$$\varphi_e(t) = \frac{2\pi}{\Phi_0} \Phi_e(t), \tag{A10c}$$

to obtain the Hamiltonian operator

$$\hat{H} = E_{C_{\Sigma}} \hat{n}^2 + \frac{(C_l m_r + C_r m_l)}{C_{\Sigma}} \dot{\varphi}_e(t) \hat{n} + U(\varphi_e(t)). \tag{A11}$$

Here we made use of  $\hbar = 1$ . The parametrisation of the model can be simplified by assuming  $m_{\Delta} = 1$ ,  $C_l = C_r$ ,  $C_{\Sigma} = C$  and  $m_r = -\beta$ . With these assumptions, we can express the Hamiltonian as

$$\hat{H} = E_C \hat{n}^2 + \left(\frac{1}{2} - \beta\right) \dot{\varphi}_e(t) \hat{n} + U\left(\varphi_e(t)\right). \tag{A12}$$

The next step in the derivation of the circuit Hamiltonian Eq. (4) is to add a linear drive term of the form

 $n_g(t)\hat{n}$  to the model. In Fig. 11 we display a modified circuit. The circuit shown in Fig. 11 contains an additional branch with a voltage source modelled with the real-valued function  $V_g(t)$  and a coupling capacitor with the capacitance  $C_g$ . Note that we model the voltage source also as an EMF.

Kirchhoff's voltage law for the central loop

$$V_{C_q} + V_q(t) = V_{C_l},$$
 (A13)

can be used to obtain the circuit Hamiltonian  $\hat{H}^*$  for the system displayed in Fig. 11 by making use of the previously obtained results for the circuit displayed in Fig. 10.

The Lagrangian  $\mathcal{L}^*$  of the modified system reads

$$\mathcal{L}^* = \mathcal{L} + \frac{C_g}{2} \left( \dot{\Phi}_l(t) - V_g(t) \right)^2. \tag{A14}$$

Therefore,  $\mathcal{L}^*$  can also be expressed in terms of the variable  $\Phi(t)$ . If we evaluate the square in Eq. (A14), we find

$$\mathcal{L}^* = \mathcal{L} + \frac{C_g}{2m_{\Delta}^2} \Phi(t)^2 - \frac{C_g}{m_{\Delta}^2} \dot{\Phi}(t) \left( m_r \dot{\Phi}_e(t) + m_{\Delta} V_g(t) \right), \tag{A15}$$

where we neglect all factors which only contribute a non-measurable global phase factors to the time evolution of the system. As before, we simplify the parametrisation. Assuming  $m_{\Delta}=1,\ C_l=C_r,\ C=C_{\Sigma}$  and  $m_r=-\beta,$  yields

$$\mathcal{L}^* = \frac{(C + C_g)}{2} \dot{\Phi}(t)^2 - \left(\frac{C}{2} - \beta \left(C + C_g\right)\right) \dot{\Phi}_e(t) \dot{\Phi}(t)$$
$$- C_g V_g(t) \dot{\Phi}(t) - U\left(\Phi(t)\right), \tag{A16}$$

where we also neglected factors which in the end only contribute a non-measurable global phase factors to the time evolution of the system. Next, in an ad hoc manner, we make the assumption that  $C+C_g\to C$  in such a way that the system's time evolution can be modelled with the Lagrangian

$$\mathcal{L}^* = \frac{C}{2}\dot{\Phi}(t)^2 - C\left(\frac{1}{2} - \beta\right)\dot{\Phi}_e(t)\dot{\Phi}(t) - C_gV_g(t)\dot{\Phi}(t) - U\left(\Phi(t)\right). \tag{A17}$$

This allows us to express the conjugate variable as

$$Q = C\dot{\Phi}(t) - C\left(\frac{1}{2} - \beta\right)\dot{\Phi}_e(t) - C_gV_g(t). \tag{A18}$$

Consequently, the first part of the Hamiltonian function reads

$$Q\dot{\Phi}(t) = \frac{Q^2}{C} + \left(\frac{1}{2} - \beta\right)\dot{\Phi}_e(t)Q + \frac{C_g}{C}V_g(t)Q \quad (A19)$$

and the second part of the Hamiltonian function can be expressed as

$$\mathcal{L}^* = \frac{Q^2}{2C} - U(\Phi(t)), \tag{A20}$$

where all factors which only contribute a non-measurable global phase factors to the time evolution of the system are neglected. Therefore, adding both parts yields

$$H^* = E_C \left(\frac{Q}{2e}\right)^2 + \left(\frac{1}{2} - \beta\right) (2e)\dot{\Phi}_e(t) \left(\frac{Q}{2e}\right)$$

$$-2E_C n_g(t) \left(\frac{Q}{2e}\right) + U\left(\Phi(t)\right),$$
(A21)

where the real-valued function  $n_q(t)$  is defined as

$$n_g(t) = -\frac{C_g V_g(t)}{2e}. (A22)$$

As before, we use  $\hbar = 1$  to simplify the Hamiltonian.

If we promote the conjugate variables to conjugate operators, complete the square with regard to the external charge variable, make use of the substitutions in Eq. (A10)(a-c) and drop all terms which only contribute non-measurable global phase factors to the time evolution of the system, we obtain the result

$$\hat{H}^* = E_C \left( \hat{n} - n_g(t) \right)^2 + \left( \frac{1}{2} - \beta \right) \dot{\varphi}_e(t) \hat{n}$$

$$- E_{J,l} \cos \left( \hat{\varphi} + \beta \varphi_e(t) \right)$$

$$- E_{J,r} \cos \left( \hat{\varphi} + (\beta - 1) \varphi_e(t) \right). \tag{A23}$$

In the main text we use the Hamiltonian Eq. (A23) to model flux-tunable transmons. Note that in the main text we omit the labels e and g in the real-valued functions  $n_q(t)$  and  $\varphi_e(t)$ .

### Appendix B: Detailed discussion of the effective Hamiltonian

In this appendix, we provide a detailed discussion of the effective Hamiltonian Eq. (7) we use to obtain the results in Sec. IV E. Note that we use  $\hbar = 1$  throughout this work.

The effective Hamiltonian we use to model our NIGQCs, is defined as

$$\hat{H}_{\text{Eff.}} = \hat{H}_{\text{Res.},\Sigma} + \hat{H}_{\text{Tun.eff.},\Sigma} + \hat{D}_{\text{Charge}} + \hat{\mathcal{D}}_{\text{Flux}} + \hat{W}_{\text{Int.}}.$$
(B1)

The first term

$$\hat{H}_{\mathrm{Res.},\Sigma} = \sum_{k \in K} \omega_k^{(R)} \hat{a}_k^{\dagger} \hat{a}_k, \tag{B2}$$

describes a collection of non-interacting resonators. Here  $K\subseteq\mathbb{N}^0$  denotes an index set for the resonators and  $\omega_k^{(R)}$  refers to the different resonator frequencies. The operators  $\hat{a}$  and  $\hat{a}^\dagger$  are the bosonic annihilation and creation operators. We use the basis states of the time-independent harmonic oscillator, see Ref. [35, Section 2.5], as the basis states for our simulations.

The second term

$$\hat{H}_{\text{Tun.eff.},\Sigma} = \sum_{j \in J} \omega_j^{(q)}(t) \hat{b}_j^{\dagger} \hat{b}_j + \frac{\alpha_j^{(q)}(t)}{2} \left( \hat{b}_j^{\dagger} \hat{b}_j \left( \hat{b}_j^{\dagger} \hat{b}_j - \hat{I} \right) \right), \tag{B3}$$

describes a collection of non-interacting flux-tunable transmons which are modelled as adiabatic, anharmonic oscillators. The operators  $\hat{b}$  and  $\hat{b}^{\dagger}$  are the bosonic annihilation and creation operators. The function

$$\omega_j^{(q)}(t) = \sqrt{2E_{C_j}E_{J_{\text{eff.,}j}}(t)} - \frac{E_{C_j}}{4}\sum_{n=0}^{24}a_n\Xi(t)^n,$$
 (B4)

is used to model the flux-tunable transmon qubit frequency. Here  $a_n$  are real-valued constants and  $E_{C_j}$  and  $E_{J_{\mathrm{eff},j}}(t)$  are the capacitive and effective Josephson energies for the transmon qubits, respectively. The latter is defined as

$$E_{J_{\text{eff.},j}}(t) = E_{\Sigma,j} \sqrt{\cos\left(\frac{\varphi_j(t)}{2}\right)^2 + d_j^2 \sin\left(\frac{\varphi_j(t)}{2}\right)^2},$$
(B5)

where  $d_j = (E_{J_{r,j}} - E_{J_{l,j}})/(E_{J_{r,j}} + E_{J_{l,j}})$ . The function  $\Xi_j(t)$  in Eq. (B4) is defined as

$$\Xi_j(t) = \sqrt{\frac{E_{C_j}}{2E_{J_{\text{eff.},j}}(t)}}.$$
 (B6)

Furthermore, we define the flux-tunable anharmonicity as

$$\alpha_j^{(q)}(t) = -\frac{E_{C_j}}{4} \sum_{n=0}^{24} b_n \Xi(t)^n,$$
 (B7)

where the different  $b_n$  are real-valued constants. We emphasise that Eqs. (B4) and (B7) are taken from Ref. [25]. The functions in Eqs. (B4) and (B7) are used to approximate the lowest three eigenvalues of the circuit Hamiltonian Eq. (4). In Ref. [18, Appendix B] the authors asses and discuss the accuracy of this approximation.

We use the time-dependent harmonic basis states

$$\psi^{(m)}(x(t)) = \frac{1}{\sqrt{2^m m!}} \left(\frac{\xi(t)}{\pi}\right)^{\frac{1}{4}} e^{-\frac{x^2(t)}{2}} \mathcal{H}_m(x(t)), \quad (B8)$$

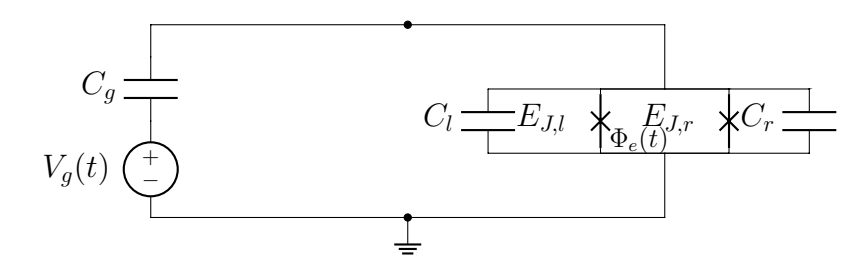


FIG. 11. Illustration of a lumped-element circuit. The right branch contains two linear capacitors with capacitances  $C_l$  (left) and  $C_r$  (right), two Josephson junctions with Josephson energies  $E_{J,l}$  (left) and  $E_{J,r}$  (right) and an external flux  $\Phi_e(t)$  threading through the loop between the two Josephson junctions. The left branch contains a linear capacitor with capacitance  $C_g$  and a voltage source  $V_g(t)$ . As it is common practice, we mark the ground node by a dashed triangle.

of the time-dependent harmonic oscillator

$$\hat{H} = E_C \hat{n}^2 + \frac{E_{J,\text{eff}}(t)}{2} \left(\hat{\varphi} - \varphi_{\text{eff}}(t)\right)^2, \quad (B9)$$

as the basis states for our simulations of the effective fluxtunable transmons. Additionally, we define the auxiliary functions

$$\xi(t) = (E_{J,\text{eff}}(t)/2E_C)^{1/2}$$
 (B10a)

$$x(t) = \sqrt{\xi(t)}(\varphi - \varphi_{\text{eff}}(t))$$
 (B10b)

$$\varphi_{\text{eff.}}(t) = \arctan\left(d\tan\left(\frac{\varphi(t)}{2}\right)\right),$$
 (B10c)

and note that  $\mathcal{H}_m$  denotes the Hermite polynomial of order  $m \in \mathbb{N}^0$ .

The third term

$$\hat{D}_{\text{Charge}} = \sum_{j \in J} \Omega_j(t) \left( \hat{b}_j^{\dagger} + \hat{b}_j \right), \tag{B11}$$

describes a charge drive. Here  $\Omega_j(t) \propto -2E_{C_j}n_j(t)$  and we approximate the charge operators  $\hat{n}_j$  by effective charge operators  $\hat{n}_{j,\text{eff.}}$  which can be expressed in terms of the bosonic annihilation and creation operators, see Ref. [22].

The fourth term

$$\hat{\mathcal{D}}_{\text{Flux}} = \sum_{j \in J} -i\sqrt{\frac{\xi_{j}(t)}{2}} \dot{\varphi}_{\text{eff.},j}(t) \left(\hat{b}_{j}^{\dagger} - \hat{b}_{j}\right) + \sum_{j \in J} \frac{i}{4} \frac{\dot{\xi}_{j}(t)}{\xi_{j}(t)} \left(\hat{b}_{j}^{\dagger} \hat{b}_{j}^{\dagger} - \hat{b}_{j} \hat{b}_{j}\right),$$
(B12)

describes a nonadiabatic flux drive. We find

$$\varphi_{\text{eff},j}(t) = \dot{\varphi}_{j}(t) \frac{d_{j}}{2\left(\cos\left(\frac{\varphi_{j}(t)}{2}\right)^{2} + d_{j}^{2}\sin\left(\frac{\varphi_{j}(t)}{2}\right)^{2}\right)}$$
(B13)

and

$$\frac{\dot{\xi}_{j}(t)}{\xi_{j}(t)} = \dot{\varphi}_{j}(t) \frac{(d_{j}^{2} - 1)\sin(\varphi_{j}(t))}{8\left(\cos\left(\frac{\varphi_{j}(t)}{2}\right)^{2} + d_{j}^{2}\sin\left(\frac{\varphi_{j}(t)}{2}\right)^{2}\right)}.$$
(B14)

TABLE VI. Device parameters for the system illustrated in Fig. 12. The units are the same as for the parameters in Table I. The device parameters are motivated by the experiments discussed in Ref. [53].

i	$\omega_i^{(Q)}/2\pi$	$\alpha_i^{(Q)}/2\pi$	$E_{C_i}/2\pi$	$E_{J_{l,i}}/2\pi$	$E_{J_{r,i}}/2\pi$	$\varphi_{0,i}/2\pi$
0	5.100	-0.310	1.079	13.446	0	0
1	6.200	-0.285	1.027	20.371	0	0
2	8.100	-0.235	0.880	17.905	21.486	0.075

The term in Eq. (B12) results from the fact that we model the effective flux-tunable transmon in a time-dependent basis. Therefore, for the time-dependent Schrödinger equation to stay form invariant a time-dependent basis transformation term is needed, see Ref. [18].

The fifth term

$$\hat{W}_{\text{Int.}} = \sum_{(k,j)\in K\times J} g_{k,j}^{(a,b)}(t) \left( \hat{a}_k^{\dagger} + \hat{a}_k \right) \otimes \left( \hat{b}_j^{\dagger} + \hat{b}_j \right), \tag{B15}$$

describes time-dependent dipole-dipole interactions. As before, the time dependence of the interaction strength

$$g_{k,j}^{(a,b)}(t) = G_{k,j} \sqrt[4]{\frac{E_{J_{\text{eff.,j}}}(t)}{8E_{C_j}}},$$
 (B16)

is a result of the fact that we model the effective fluxtunable transmon in a time-dependent basis, see Ref. [18]. This time-dependent interaction strength model is motivated by the work in Ref. [22].

The relation between the effective and the circuit model is discussed in Ref. [18].

### Appendix C: Simulations of the parametric coupler device architecture

In the main text, in Sec. IV E, we investigated the influence of the adiabatic approximation on gate-error trajectories obtained with the effective Hamiltonian Eq. (7) for the device architecture illustrated in Figs. 1(a-c). Here the adiabatic approximation was applied to one effective

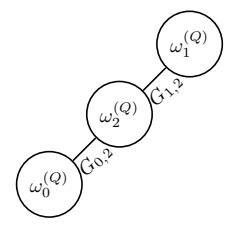


FIG. 12. Illustrations of fixed-frequency transmon qubits with qubit frequencies  $\omega_0^{(Q)}$  and  $\omega_1^{(Q)}$  and a flux-tunable transmon with park frequency  $\omega_2^{(Q)}$  which constitute a non-ideal gate-based transmon quantum computer (NIGQC) with two qubits. The Hamiltonian we use to model the dynamics of our NIGQC is given by Eq. (7). The device parameters we use to specify the Hamiltonian are listed in Table VI. The control pulses we use to implement the gate is given by Eq. (C1).

TABLE VII. Control pulse parameters for the implementation of a  $CZ_{0,1}$  two-qubit gate on a two-qubit NIGQC as illustrated in Fig. 12. We use the parameters to specify the microwave pulse given by Eq. (C1). The first column shows the gate we implement. The second column shows the rise and fall time  $T_{r/f}$  in ns. The third column shows the pulse duration without buffer time  $T_p$  in ns. The fourth column shows the pulse duration with buffer time  $T_d$  in ns. The fifth column shows the unit-less pulse amplitude  $\delta$ . The sixth column shows the drive frequency  $\omega^{(D)}$  in GHz. We use the **effective Hamiltonian** Eq. (7) to obtain the parameters listed in this table.

Gate	$T_{ m r/f}$	$T_p$	$T_d$	$\delta/2\pi$	$\omega^{(D)}/2\pi$
$CZ_{0,1}$	24.674	299.406	304.406	0.082	0.808

flux-tunable transmon only. In this appendix, we perform analogous simulations for a different device architecture studied in Refs. [46, 48, 49, 53, 64]. Here we use a flux microwave pulse to implement two-qubit CZ gates.

The device architecture is illustrated in Fig. 12 and the device parameters are listed in Table VI. The interaction strength G is set to 85 MHz for all simulations, see Appendix B. Here we couple two fixed-frequency transmons with qubit frequencies  $\omega_0^{(Q)}$  and  $\omega_1^{(Q)}$  by means of a fluxtunable transmon with park frequency  $\omega_2^{(Q)}$ . We use the control pulse

$$\varphi(t) = \varphi_0 + \delta e(t) \cos(\omega^{(D)}t),$$
 (C1)

for the external flux  $\varphi(t)$  to implement a sequence of CZ gates. The real-valued function e(t) is an envelope function,  $\delta$  is the pulse amplitude,  $\omega^{(D)}$  is the drive frequency and  $\varphi_0$  denotes the flux offset. Since the flux offset defines an operating point for the device, we list the parameter in Table VI. The envelope function is defined as

$$e(t) = \begin{cases} \sin(\lambda t) & \text{if } 0 \le t < T_{\text{r/f}} \\ 1 & \text{if } T_{\text{r/f}} \le t \le \Delta T \\ \sin(\frac{\pi}{2} + \lambda(t - \Delta T)) & \text{if } \Delta T < t \le T_p, \end{cases}$$
 (C2)

where  $T_{\rm r/f}$  denotes the rise and fall time,  $\lambda = \pi/(2T_{\rm r/f})$  and  $\Delta T = T_p - T_{\rm r/f}$ . Note that in the computer program

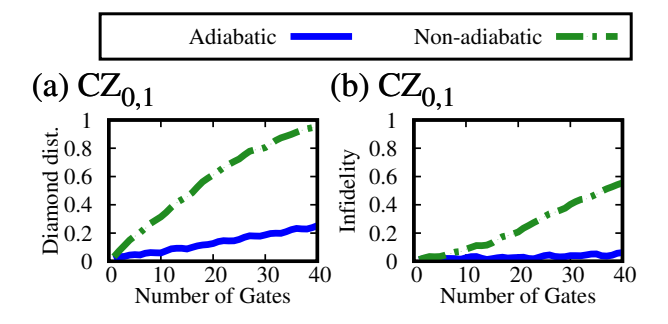


FIG. 13. (Color Online) Gate errors as functions of the number of gates for a program which executes forty CZ gates in a row. In (a) we show the diamond distance and in (b) we show the average infidelity. We run the program on the twoqubit NIGQC illustrated in Fig. 12. The results are obtained with the **effective Hamiltonian** Eq. (2) and the device parameters listed in Table VI. We run the program two times on each NIGQC. On the first run, we model the flux-tunable transmons as adiabatic qubits. These results are displayed as a blue solid line. On the second run, we model the fluxtunable transmons as nonadiabatic qubits. These results are displayed as a green dashed line. We can observe that the gate-error trajectories for the two cases can deviate up to 0.8 for the diamond distance and 0.6 for the average infidelity. Furthermore, we can observe that the gate-error trajectories for both cases exhibit rather different qualitative behaviour.

we add an additional free time evolution (the buffer time) to the pulse such that the complete pulse duration  $T_d$  is 5 ns longer than  $T_p$ . The pulse parameters for the pulse we use to obtain the results in this appendix are listed in Table VII. Note that we use single-qubit z-axis rotations  $R_i^{(z)}(\phi_i)$  for every qubit to improve the gate performance.

Figures 13(a-b) show the diamond distance  $\mu_{\diamond}(a)$  and the average infidelity  $\mu_{\rm IF_{avg}}(b)$  as functions of the number of gates for the two-qubit NIGQC illustrated in Fig. 12. Here we executed a program which consists of forty CZ gates in a row. In each panel we show the results for the two different cases; adiabatic regime (blue solid) and nonadiabatic regime (green dashed).

As one can see, for the adiabatic case we find smaller gate errors and a smaller increase in gate errors over time. Furthermore, after forty CZ gate repetitions we find that the diamond distances deviate up to 0.8 and the average infidelities differ by about 0.6. Consequently, we find that neglecting the flux drive term in Eq. (10) leads to substantial deviations between the two NIGQC models.

Prototype gate-based quantum computers with similar device parameters are discussed in Refs. [46, 48, 49, 53, 64]. To the best knowledge of the authors, we find that most models which theoretically describe this device architecture model flux-tunable transmons adiabatically.

TABLE VIII. Control pulse parameters for the implementation of  $R^{(x)}(\pi/2)$  rotations on a two-qubit NIGQC as illustrated in Fig. 1(a). We use the parameters to specify the microwave pulse given by Eq. (12). The first column shows the gate we implement. The second column shows the pulse duration  $T_d$  in ns. The third column shows the drive frequency  $\omega^{(D)}$  in GHz. The fourth column shows the pulse amplitude a as a unit-less quantity. The fifth column shows the envelope function parameter  $\sigma$  in ns. The sixth column shows the DRAG amplitude b in ns. We use the **circuit Hamiltonian** Eq. (2) to obtain the parameters listed in this table.

Gate	$T_d$	$\omega^{(D)}/2\pi$	a	$\sigma$	b
$R_0^{(x)}(\pi/2)$	52.250	4.196	0.004	12.082	0.072
$R_1^{(x)}(\pi/2)$	52.950	5.195	0.005	10.000	0.070

TABLE IX. Control pulse parameters for the implementation of CZ gates on a two-qubit NIGQC as illustrated in Fig. 1(a). We use the parameters to specify the unimodal pulse (UMP) given by Eq. (13). The first column shows the gate we implement. The second column shows the pulse type. The third column shows the pulse time parameter  $T_p$  in ns. The fourth column shows the pulse duration  $T_d$  in ns. The fifth column shows the unit-less pulse amplitude  $\delta$ . The sixth column shows the rise and fall parameter  $\sigma$  in ns. We use the **circuit Hamiltonian** Eq. (2) to obtain the parameters listed in this table.

Gate	Pulse	$T_p$	$T_d$	$\delta/2\pi$	$\sigma$
$\mathrm{CZ}_{0,1}$	UMP	99.835	125.000	0.392	1.313

### Appendix D: Tables with control pulse parameters and gate-error quantifiers

In this appendix, we provide the control pulse parameters listed in Tables VIII–XIX which we use to obtain the results in Sec. IV and the gate-error metrics listed in Tables XX–XXV we use to obtain Fig. 5.

The control pulse parameters for the circuit Hamiltonian Eq. (2) NIGQC model are listed in Tables VIII–XIII. Similarly, the control pulse parameters for the effective Hamiltonian Eq. (7) NIGQC model are listed in Tables XIV–XIX.

The gate-error metrics for the circuit Hamiltonian Eq. (2) NIGQC model are provided in Tables XX–XXII. Similarly, the gate-error metrics for the effective Hamiltonian Eq. (7) NIGQC model are listed in Tables XXIII–XXV

TABLE X. Control pulse parameters for the implementation of  $R^{(x)}(\pi/2)$  rotations on a three-qubit NIGQC as illustrated in Fig. 1(b). The units are the same as in Table VIII. We use the **circuit Hamiltonian** Eq. (2) to obtain the parameters listed in this table.

Gate	$T_d$	$\omega^{(D)}/2\pi$	a	$\sigma$	b
$R_0^{(x)}(\pi/2)$	52.250	4.196	0.004	12.093	0.168
$R_1^{(x)}(\pi/2)$	52.950	5.190	0.004	9.997	0.067
$R_2^{(x)}(\pi/2)$	52.950	5.695	0.004	10.011	0.066

TABLE XI. Control pulse parameters for the implementation of CZ gates on a three-qubit NIGQC as illustrated in Fig. 1(b). The units are the same as in Table IX. We use the effective Hamiltonian Eq. (2) to obtain the parameters listed in this table.

Gate	Pulse	$T_p$	$T_d$	$\delta/2\pi$	$\sigma$
$CZ_{0,1}$	UMP	96.026	125.000	0.391	1.823
$CZ_{1,2}$	UMP	75.367	110.000	0.276	0.513

TABLE XII. Control pulse parameters for the implementation of  $R^{(x)}(\pi/2)$  rotations on a four-qubit NIGQC as illustrated in Fig. 1(c). The units are the same as in Table VIII. We use the **circuit Hamiltonian** Eq. (2) to obtain the parameters listed in this table.

Gate	$T_d$	$\omega^{(D)}/2\pi$	a	$\sigma$	b
$R_0^{(x)}(\pi/2)$	52.250	4.193	0.004	12.378	0.047
$R_1^{(x)}(\pi/2)$	52.950	5.190	0.004	10.255	0.063
$R_2^{(x)}(\pi/2)$	52.950	5.689	0.004	10.312	0.065
$R_3^{(x)}(\pi/2)$	52.950	4.951	0.005	10.191	0.012

TABLE XIII. Control pulse parameters for the implementation of CZ gates on a four-qubit NIGQC as illustrated in Fig. 1(c). The units are the same as in Table IX. We use the circuit Hamiltonian Eq. (2) to obtain the parameters listed in this table.

Gate	Pulse	$T_p$	$T_d$	$\delta/2\pi$	σ
$CZ_{0,1}$	UMP	100.241	125.000	0.392	1.283
$CZ_{1,2}$	UMP	68.046	90.000	0.275	0.182
$CZ_{2,3}$	UMP	80.500	94.000	0.320	0.500
$\mathrm{CZ}_{0,3}$	UMP	97.708	116.000	0.353	1.458

TABLE XIV. Control pulse parameters for the implementation of  $R^{(x)}(\pi/2)$  rotations on a two-qubit NIGQC as illustrated in Fig. 1(a). We use the parameters to specify the microwave pulse given by Eq. (12). The first column shows the gate we implement. The second column shows the pulse duration  $T_d$  in ns. The third column shows the drive frequency  $\omega^{(D)}$  in GHz. The fourth column shows the pulse amplitude a as a unit-less quantity. The fifth column shows the envelope function parameter  $\sigma$  in ns. The sixth column shows the DRAG amplitude b in ns. We use the **effective Hamiltonian** Eq. (7) to obtain the parameters listed in this table.

Gate	$T_d$	$\omega^{(D)}/2\pi$	a	$\sigma$	b
$R_0^{(x)}(\pi/2)$	52.250	4.196	0.058	12.082	0.072
$R_1^{(x)}(\pi/2)$	52.950	5.195	0.065	10.000	0.070

TABLE XV. Control pulse parameters for the implementation of CZ gates on a two-qubit NIGQC as illustrated in Fig. 1(a). We use the parameters to specify the unimodal pulse (UMP) and bimodal pulse (BMP) given by Eqs. (13) and (14), respectively. The first column shows the gate we implement. The second column shows the pulse type. The third column shows the pulse time parameter  $T_p$  in ns. The fourth column shows the pulse duration  $T_d$  in ns. The fifth column shows the unitless pulse amplitude  $\delta$ . The sixth column shows the rise and fall parameter  $\sigma$  in ns. We use the **effective Hamiltonian** Eq. (7) to obtain the parameters listed in this table.

Gate	Pulse	$T_p$	$T_d$	$\delta/2\pi$	$\sigma$
$CZ_{0,1}$	UMP	87.258	95.000	0.391	0.459
$\operatorname{CZ}_{0,1}$	BMP	88.570	95.000	0.392	0.394

TABLE XVI. Control pulse parameters for the implementation of  $R^{(x)}(\pi/2)$  rotations on a three-qubit NIGQC as illustrated in Fig. 1(b). The units are the same as in Table XIV. We use the **effective Hamiltonian** Eq. (7) to obtain the parameters listed in this table.

Gate	$T_d$	$\omega^{(D)}/2\pi$	a	σ	b
$R_0^{(x)}(\pi/2)$	52.250	4.196	0.058	12.082	0.072
$R_1^{(x)}(\pi/2)$	52.950	5.189	0.065	10.000	0.070
$R_2^{(x)}(\pi/2)$	52.950	5.694	0.066	9.990	0.032

TABLE XVII. Control pulse parameters for the implementation of CZ gates on a three-qubit NIGQC as illustrated in Fig. 1(b). The units are the same as in Table XV. We use the effective Hamiltonian Eq. (7) to obtain the parameters listed in this table.

Gate	Pulse	$T_p$	$T_d$	$\delta/2\pi$	$\sigma$
$CZ_{0,1}$	UMP	87.252	95.006	0.391	0.494
$CZ_{0,1}$	BMP	90.057	92.188	0.391	0.420
$\mathrm{CZ}_{1,2}$	UMP	68.831	80.000	0.276	0.554

TABLE XVIII. Control pulse parameters for the implementation of  $R^{(x)}(\pi/2)$  rotations on a four-qubit NIGQC as illustrated in Fig. 1(c). The units are the same as in Table XIV. We use the **effective Hamiltonian** Eq. (7) to obtain the parameters listed in this table.

Gate	$T_d$	$\omega^{(D)}/2\pi$	a	$\sigma$	b
$R_0^{(x)}(\pi/2)$	52.250	4.191	0.058	12.082	0.072
$R_1^{(x)}(\pi/2)$	52.950	5.189	0.065	10.000	0.070
$R_2^{(x)}(\pi/2)$	52.950	5.688	0.066	9.990	0.032
$R_3^{(x)}(\pi/2)$	52.950	4.950	0.066	9.990	0.032

TABLE XIX. Control pulse parameters for the implementation of CZ gates on a four-qubit NIGQC as illustrated in Fig. 1(c). The units are the same as in Table XV. We use the **effective Hamiltonian** Eq. (7) to obtain the parameters listed in this table.

Gate	Pulse	$T_p$	$T_d$	$\delta/2\pi$	$\sigma$
$CZ_{0,1}$	UMP	87.254	95.013	0.391	0.453
$\mathrm{CZ}_{0,1}$	BMP	89.925	98.114	0.392	0.400
$CZ_{1,2}$	UMP	67.802	115.238	0.275	0.338
$CZ_{2,3}$	UMP	71.620	98.197	0.320	0.543
${\rm CZ}_{0,3}$	UMP	92.616	124.768	0.353	1.877

TABLE XX. Gate-error quantifiers for  $R^{(x)}(\pi/2)$  rotations and CZ gates for a two-qubit NIGQC as illustrated in Fig. 1(a). The gate-error quantifiers are obtained with the **circuit Hamiltonian** Eq. (2), the device parameters listed in Table I and the pulse parameters listed in Tables VIII and IX. The first column shows the target gate. The second column shows the pulse type, see Figs. 2(a-c). The third column shows the diamond distance  $\mu_{\Diamond}$  given by Eqs. (28) and (29). The fourth column shows the average infidelity  $\mu_{\mathrm{IF}_{\mathrm{avg}}}$  given by Eq. (24). The fifth column shows the leakage measure  $\mu_{\mathrm{Leak}}$  given by Eq. (26).

Gate	Pulse	$\mu_{\diamond}$	$\mu_{ m IF}_{ m avg}$	$\mu_{ m Leak}$
$R_0^{(x)}(\pi/2)$	MP	0.0093	0.0004	0.0004
$R_1^{(x)}(\pi/2)$	MP	0.0080	0.0004	0.0004
$CZ_{0,1}$	UMP	0.0290	0.0011	0.0008

TABLE XXI. Gate-error quantifiers for  $R^{(x)}(\pi/2)$  rotations and CZ gates for a three-qubit NIGQC as illustrated in Fig. 1(b). The gate-error quantifiers are obtained with the **circuit Hamiltonian** Eq. (2), the device parameters listed in Table I and the pulse parameters listed in Tables X and XI. The rows and columns show the same unit-less quantities as Table XX.

Gate	Pulse	$\mu_{\diamond}$	$\mu_{ m IF}_{ m avg}$	$\mu_{ m Leak}$
$R_0^{(x)}(\pi/2)$	MP	0.044	0.003	0.002
$R_1^{(x)}(\pi/2)$	MP	0.038	0.002	0.001
$R_2^{(x)}(\pi/2)$	MP	0.039	0.002	0.001
$CZ_{0,1}$	UMP	0.044	0.010	0.010
$CZ_{1,2}$	UMP	0.012	0.002	0.002

TABLE XXII. Gate-error quantifiers for  $R^{(x)}(\pi/2)$  rotations and CZ gates for a four-qubit NIGQC as illustrated in Fig. 1(c). The gate-error quantifiers are obtained with the **circuit Hamiltonian** Eq. (2), the device parameters listed in Table I and the pulse parameters listed in Tables XII and XIII. The rows and columns show the same unit-less quantities as Table XX.

Gate	Pulse	$\mu_{\diamond}$	$\mu_{ ext{IF}_{ ext{avg}}}$	$\mu_{ m Leak}$
$R_0^{(x)}(\pi/2)$	MP	0.058	0.004	0.002
$R_1^{(x)}(\pi/2)$	MP	0.054	0.003	0.002
$R_2^{(x)}(\pi/2)$	MP	0.053	0.003	0.002
$R_3^{(x)}(\pi/2)$	MP	0.057	0.004	0.002
$CZ_{0,1}$	UMP	0.031	0.005	0.004
$CZ_{1,2}$	UMP	0.144	0.029	0.018
$CZ_{2,3}$	UMP	0.073	0.008	0.005
$CZ_{0,3}$	UMP	0.046	0.005	0.003

TABLE XXIII. Gate-error quantifiers for  $R^{(x)}(\pi/2)$  rotations and CZ gates for a two-qubit NIGQC as illustrated in Fig. 1(a). The gate-error quantifiers are obtained with the **effective Hamiltonian** Eq. (7), the device parameters listed in Table I and the pulse parameters listed in Tables XIV and XV. The first column shows the target gate. The second column shows the pulse type, see Figs. 2(a-c). The third column shows the diamond distance  $\mu_{\Diamond}$  given by Eqs. (28) and (29). The fourth column shows the average infidelity  $\mu_{\mathrm{IF}_{\mathrm{avg}}}$  given by Eq. (24). The fifth column shows the leakage measure  $\mu_{\mathrm{Leak}}$  given by Eq. (26).

Gate	Pulse	$\mu_{\diamond}$	$\mu_{ ext{IF}_{ ext{avg}}}$	$\mu_{ m Leak}$
$R_0^{(x)}(\pi/2)$	MP	0.0089	0.0004	0.0004
$R_1^{(x)}(\pi/2)$	MP	0.0090	0.0004	0.0004
$CZ_{0,1}$	UMP	0.0424	0.0012	0.0005
$CZ_{0,1}$	BMP	0.0167	0.0006	0.0005

TABLE XXIV. Gate-error quantifiers for  $R^{(x)}(\pi/2)$  rotations and CZ gates for a three-qubit NIGQC as illustrated in Fig. 1(b). The gate-error quantifiers are obtained with the **effective Hamiltonian** Eq. (7), the device parameters listed in Table I and the pulse parameters listed in Tables XVI and XVII. The rows and columns show the same unit-less quantities as Table XXIII.

Gate	Pulse	$\mu_{\diamond}$	$\mu_{ m IF}_{ m avg}$	$\mu_{ m Leak}$
$R_0^{(x)}(\pi/2)$	MP	0.046	0.003	0.002
$R_1^{(x)}(\pi/2)$	MP	0.040	0.002	0.002
$R_2^{(x)}(\pi/2)$	MP	0.039	0.002	0.002
$\mathrm{CZ}_{0,1}$	UMP	0.057	0.003	0.002
$\mathrm{CZ}_{0,1}$	BMP	0.031	0.004	0.004
$CZ_{1,2}$	UMP	0.028	0.006	0.006

TABLE XXV. Gate-error quantifiers for  $R^{(x)}(\pi/2)$  rotations and CZ gates for a four-qubit NIGQC as illustrated in Fig. 1(c). The gate-error quantifiers are obtained with the **effective Hamiltonian** Eq. (7), the device parameters listed in Table I and the pulse parameters listed in Tables XVIII and XIX. The rows and columns show the same unit-less quantities as Table XXIII.

Gate	Pulse	$\mu_{\diamond}$	$\mu_{ m IF}_{ m avg}$	$\mu_{ m Leak}$
$R_0^{(x)}(\pi/2)$	MP	0.060	0.004	0.003
$R_1^{(x)}(\pi/2)$	MP	0.056	0.003	0.002
$R_2^{(x)}(\pi/2)$	MP	0.054	0.003	0.002
$R_3^{(x)}(\pi/2)$	MP	0.060	0.004	0.002
$CZ_{0,1}$	UMP	0.051	0.004	0.003
$CZ_{0,1}$	BMP	0.041	0.004	0.004
$\mathrm{CZ}_{1,2}$	UMP	0.146	0.015	0.005
$CZ_{2,3}$	UMP	0.078	0.010	0.007
$CZ_{0,3}$	UMP	0.058	0.005	0.003

- [1] M. A. Nielsen and I. L. Chuang, Quantum Computation and Quantum Information: 10th Anniversary Edition (Cambridge University Press, 2011).
- [2] J. Watrous, The Theory of Quantum Information (Cambridge University Press, 2018).
- [3] D. Willsch, M. Nocon, F. Jin, H. DeRaedt, and K. Michielsen, Physical Review A 96, 062302 (2017).
- [4] K. Michielsen, M. Nocon, D. Willsch, F. Jin, T. Lippert, and H. De Raedt, Computer Physics Communications 220, 44 (2017).
- [5] M. A. Nielsen, Physics Letters A 303, 249 (2002).
- [6] F. Jin, D. Willsch, M. Willsch, H. Lagemann, K. Michielsen, and H. De Raedt, Journal of the Physical Society of Japan 90, 012001 (2021), https://doi.org/10.7566/JPSJ.90.012001.
- [7] A. Y. Kitaev, Russian Mathematical Surveys 52, 1191 (1997).
- [8] Y. R. Sanders, J. J. Wallman, and B. C. Sanders, New Journal of Physics 18, 012002 (2015).
- [9] M. A. Rol, F. Battistel, F. K. Malinowski, C. C. Bultink, B. M. Tarasinski, R. Vollmer, N. Haider, N. Muthusubramanian, A. Bruno, B. M. Terhal, and L. DiCarlo, Phys. Rev. Lett. 123, 120502 (2019).
- [10] M. Werninghaus, D. J. Egger, F. Roy, S. Machnes, F. K. Wilhelm, and S. Filipp, npj Quantum Information 7, 14 (2021).
- [11] S. Krinner, S. Storz, P. Kurpiers, P. Magnard, J. Heinsoo, R. Keller, J. Lütolf, C. Eichler, and A. Wallraff, EPJ Quantum Technology 6, 2 (2019).
- [12] J. J. Burnett, A. Bengtsson, M. Scigliuzzo, D. Niepce, M. Kudra, P. Delsing, and J. Bylander, npj Quantum Information 5, 54 (2019).
- [13] M. McEwen, L. Faoro, K. Arya, A. Dunsworth, T. Huang, S. Kim, B. Burkett, A. Fowler, F. Arute, J. C. Bardin, A. Bengtsson, A. Bilmes, B. B. Buckley, N. Bushnell, Z. Chen, R. Collins, S. Demura, A. R. Derk, C. Erickson, M. Giustina, S. D. Harrington, S. Hong, E. Jeffrey, J. Kelly, P. V. Klimov, F. Kostritsa, P. Laptev, A. Locharla, X. Mi, K. C. Miao, S. Montazeri, J. Mutus, O. Naaman, M. Neeley, C. Neill, A. Opremcak, C. Quintana, N. Redd, P. Roushan, D. Sank, K. J. Satzinger, V. Shvarts, T. White, Z. J. Yao, P. Yeh, J. Yoo, Y. Chen, V. Smelyanskiy, J. M. Martinis, H. Neven, A. Megrant, L. Ioffe, and R. Barends, Nature Physics 18, 107 (2022).
- [14] N. Lacroix, C. Hellings, C. K. Andersen, A. Di Paolo, A. Remm, S. Lazar, S. Krinner, G. J. Norris, M. Gabureac, J. Heinsoo, A. Blais, C. Eichler, and A. Wallraff, PRX Quantum 1, 110304 (2020).
- [15] S. Krinner, S. Lazar, A. Remm, C. Andersen, N. Lacroix, G. Norris, C. Hellings, M. Gabureac, C. Eichler, and A. Wallraff, Phys. Rev. Applied 14, 024042 (2020).
- [16] C. K. Andersen, A. Remm, S. Lazar, S. Krinner, N. Lacroix, G. J. Norris, M. Gabureac, C. Eichler, and A. Wallraff, Nature Physics 16, 875 (2020).
- [17] C. A. Balanis, Advanced Engineering Electromagnetics (Wiley, 2012).
- [18] H. Lagemann, D. Willsch, M. Willsch, F. Jin, H. De Raedt, and K. Michielsen, Phys. Rev. A 106, 022615 (2022).
- [19] H. DeRaedt, Computer Physics Reports 7, 1 (1987).
- [20] J. Huyghebaert and H. De Raedt, J. Phys. A: Math. Gen.

- **23**, 5777 (1990).
- [21] D. Willsch, M. Nocon, F. Jin, H. De Raedt, and K. Michielsen, Phys. Rev. A 96, 062302 (2017).
- [22] J. Koch, T. M. Yu, J. Gambetta, A. A. Houck, D. I. Schuster, J. Majer, A. Blais, M. H. Devoret, S. M. Girvin, and R. J. Schoelkopf, Phys. Rev. A 76, 042319 (2007).
- [23] X. You, J. A. Sauls, and J. Koch, Phys. Rev. B 99, 174512 (2019).
- [24] R.-P. Riwar and D. P. DiVincenzo, npj Quantum Information 8, 36 (2022).
- [25] N. Didier, E. A. Sete, M. P. da Silva, and C. Rigetti, Phys. Rev. A 97, 022330 (2018).
- [26] F. Motzoi, J. M. Gambetta, P. Rebentrost, and F. K. Wilhelm, Phys. Rev. Lett. 103, 110501 (2009).
- [27] D. C. McKay, C. J. Wood, S. Sheldon, J. M. Chow, and J. M. Gambetta, Phys. Rev. A 96, 022330 (2017).
- [28] A. Blais, A. L. Grimsmo, S. M. Girvin, and A. Wallraff, Rev. Mod. Phys. 93, 025005 (2021).
- [29] D. Willsch, Supercomputer simulations of transmon quantum computers, Dissertation, RWTH Aachen University (2020).
- [30] Jülich Supercomputing Centre, Journal of large-scale research facilities 5, A135 (2019).
- [31] N. Johnston, D. Kribs, and V. Paulsen, Quantum Information and Computation 9 (2009).
- [32] I. Corporation, Mkl:math kernel library.
- [33] L. DiCarlo, J. M. Chow, J. M. Gambetta, L. S. Bishop, B. R. Johnson, D. I. Schuster, J. Majer, A. Blais, L. Frunzio, S. M. Girvin, and R. J. Schoelkopf, Nature 460, 120502 (2019).
- [34] L. DiCarlo, M. D. Reed, L. Sun, B. R. Johnson, J. M. Chow, J. M. Gambetta, L. Frunzio, S. M. Girvin, M. H. Devoret, and R. J. Schoelkopf, Nature 467, 574 (2010).
- [35] S. Weinberg, Lectures on Quantum Mechanics, 2nd ed. (Cambridge University Press, 2015).
- [36] F. Hund, Zeitschrift für Physik 40, 742 (1927).
- [37] J. von Neumann and E. P. Wigner, Über merkwürdige diskrete eigenwerte, in *The Collected Works of Eugene* Paul Wigner: Part A: The Scientific Papers, edited by A. S. Wightman (Springer Berlin Heidelberg, Berlin, Heidelberg, 1993) pp. 291–293.
- [38] F. Uhlig, Coalescing eigenvalues and crossing eigencurves of 1-parameter matrix flows (2020).
- [39] U. Srinivasan and R. Kidambi, A sorting algorithm for complex eigenvalues (2020).
- [40] S. Krinner, N. Lacroix, A. Remm, A. Di Paolo, E. Genois, C. Leroux, C. Hellings, S. Lazar, F. Swiadek, J. Herrmann, G. J. Norris, C. K. Andersen, M. Müller, A. Blais, C. Eichler, and A. Wallraff, Nature 605, 669 (2022).
- [41] F. Arute, K. Arya, R. Babbush, D. Bacon, J. Bardin, R. Barends, R. Biswas, S. Boixo, F. Brandao, D. Buell, B. Burkett, Y. Chen, J. Chen, B. Chiaro, R. Collins, W. Courtney, A. Dunsworth, E. Farhi, B. Foxen, A. Fowler, C. M. Gidney, M. Giustina, R. Graff, K. Guerin, S. Habegger, M. Harrigan, M. Hartmann, A. Ho, M. R. Hoffmann, T. Huang, T. Humble, S. Isakov, E. Jeffrey, Z. Jiang, D. Kafri, K. Kechedzhi, J. Kelly, P. Klimov, S. Knysh, A. Korotkov, F. Kostritsa, D. Landhuis, M. Lindmark, E. Lucero, D. Lyakh, S. Mandrà, J. R. McClean, M. McEwen, A. Megrant, X. Mi, K. Michielsen, M. Mohseni, J. Mutus, O. Naaman,

- M. Neeley, C. Neill, M. Y. Niu, E. Ostby, A. Petukhov, J. Platt, C. Quintana, E. G. Rieffel, P. Roushan, N. Rubin, D. Sank, K. J. Satzinger, V. Smelyanskiy, K. J. Sung, M. Trevithick, A. Vainsencher, B. Villalonga, T. White, Z. J. Yao, P. Yeh, A. Zalcman, H. Neven, and J. Martinis, Nature 574, 505–510 (2019).
- [42] A. J. Baker, G. B. P. Huber, N. J. Glaser, F. Roy, I. Tsitsilin, S. Filipp, and M. J. Hartmann, Applied Physics Letters 120, 054002 (2022), https://doi.org/10.1063/5.0077443.
- [43] J. Cohen, A. Petrescu, R. Shillito, and A. Blais, Reminiscence of classical chaos in driven transmons (2022), arXiv:2207.09361 [quant-ph].
- [44] J. B. Hertzberg, E. J. Zhang, S. Rosenblatt, E. Magesan, J. A. Smolin, J.-B. Yau, V. P. Adiga, M. Sandberg, M. Brink, J. M. Chow, and J. S. Orcutt, npj Quantum Inf. 7, 129 (2021).
- [45] S. G. Johnson, The nlopt nonlinear-optimization package.
- [46] X. Gu, J. Fernández-Pendás, P. Vikstål, T. Abad, C. Warren, A. Bengtsson, G. Tancredi, V. Shumeiko, J. Bylander, G. Johansson, and A. F. Kockum, PRX Quantum 2, 040348 (2021).
- [47] N. Wittler, F. Roy, K. Pack, M. Werninghaus, A. S. Roy, D. J. Egger, S. Filipp, F. K. Wilhelm, and S. Machnes, Phys. Rev. Applied 15, 034080 (2021).
- [48] D. C. McKay, S. Filipp, A. Mezzacapo, E. Magesan, J. M. Chow, and J. M. Gambetta, Phys. Rev. Applied 6, 064007 (2016).
- [49] M. Roth, M. Ganzhorn, N. Moll, S. Filipp, G. Salis, and S. Schmidt, Phys. Rev. A 96, 062323 (2017).
- [50] F. Yan, P. Krantz, Y. Sung, M. Kjaergaard, D. L. Campbell, T. P. Orlando, S. Gustavsson, and W. D. Oliver, Phys. Rev. Applied 10, 054062 (2018).
- [51] T. Roth, R. Ma, and W. C. Chew, IEEE Antennas and Propagation Magazine, 2 (2022).
- [52] B. Foxen, C. Neill, A. Dunsworth, P. Roushan, B. Chiaro, A. Megrant, J. Kelly, Z. Chen, K. Satzinger, R. Barends, F. Arute, K. Arya, R. Babbush, D. Bacon, J. C. Bardin, S. Boixo, D. Buell, B. Burkett, Y. Chen, R. Collins, E. Farhi, A. Fowler, C. Gidney, M. Giustina, R. Graff, M. Harrigan, T. Huang, S. V. Isakov, E. Jeffrey, Z. Jiang, D. Kafri, K. Kechedzhi, P. Klimov, A. Korotkov, F. Kostritsa, D. Landhuis, E. Lucero, J. McClean, M. McEwen, X. Mi, M. Mohseni, J. Y. Mutus, O. Naa-

- man, M. Neeley, M. Niu, A. Petukhov, C. Quintana, N. Rubin, D. Sank, V. Smelyanskiy, A. Vainsencher, T. C. White, Z. Yao, P. Yeh, A. Zalcman, H. Neven, and J. M. Martinis (Google AI Quantum), Phys. Rev. Lett. **125**, 120504 (2020).
- [53] M. Ganzhorn, G. Salis, D. J. Egger, A. Fuhrer, M. Mergenthaler, C. Müller, P. Müller, S. Paredes, M. Pechal, M. Werninghaus, and S. Filipp, Phys. Rev. Research 2, 033447 (2020).
- [54] R. Alicki, M. Horodecki, P. Horodecki, and R. Horodecki, Phys. Rev. A 65, 062101 (2002).
- [55] R. Alicki, D. A. Lidar, and P. Zanardi, Phys. Rev. A 73, 052311 (2006).
- [56] B. M. Terhal and G. Burkard, Phys. Rev. A 71, 012336 (2005).
- [57] H. A. Lagemann, Real-time simulations of transmon systems with time-dependent Hamiltonian models, Dissertation, RWTH Aachen University, Aachen (2023), veröffentlicht auf dem Publikationsserver der RWTH Aachen University; Dissertation, RWTH Aachen University, 2023.
- [58] H. Lagemann, Development and implementation of a gate-based quantum computer simulator for highdimensional Hilbert spaces, Masterarbeit, RWTH Aachen (2019), masterarbeit, RWTH Aachen, 2019.
- [59] C. E. Murray, Materials Science and Engineering: R: Reports 146, 100646 (2021).
- [60] J. M. Martinis and A. Megrant, Ucsb final report for the csq program: Review of decoherence and materials physics for superconducting qubits (2014), arXiv:1410.5793 [quant-ph].
- [61] E. Farhi, J. Goldstone, and S. Gutmann, A quantum approximate optimization algorithm (2014), arXiv:1411.4028 [quant-ph].
- [62] D. Willsch, M. Willsch, F. Jin, K. Michielsen, and H. De Raedt, Computer Physics Communications 278, 108411 (2022).
- [63] W. Fenchel, Canadian Journal of Mathematics 1, 73–77 (1949).
- [64] A. Bengtsson, P. Vikstål, C. Warren, M. Svensson, X. Gu, A. F. Kockum, P. Krantz, C. Križan, D. Shiri, I.-M. Svensson, G. Tancredi, G. Johansson, P. Delsing, G. Ferrini, and J. Bylander, Phys. Rev. Applied 14, 034010 (2020).